

N72-10539

NASA TM X-62,082

NASA TECHNICAL
MEMORANDUM

NASA TM X-62,082

CASE FILE
COPY

TARGET CONTRAST CONSIDERATIONS IN MILLIMETER
WAVE RADIOMETRY FOR AIRBORNE NAVIGATION

A. Mayer

Ames Research Center
Moffett Field, Calif. 94035

August 1971

TARGET CONTRAST CONSIDERATIONS IN MILLIMETER WAVE RADIOMETRY
FOR AIRBORNE NAVIGATION

By A. Mayer

Ames Research Center, NASA, Moffett Field, California 94035

ABSTRACT

This report describes target signal requirements for aircraft navigation systems that use radiometric receivers which "map" thermally emitted power radiated by terrain or power radiated by ground-based beacons. For selected mm-wavelength bands, microwaves suffer relatively little degradation by absorption or scattering on passage through the atmosphere, despite extreme weather variations. Interest centers on 8-mm waves because of component availability, portability (small size), high image resolution, and all-weather capability at this wavelength.

Section 1 briefly introduces the idea of radiometric airborne navigation. In Section 2, elements of radiometry, terrain radiation, and atmospheric transmission characteristics are reviewed, and data pertaining to them at 8 mm wavelength are collected. In Section 3, calculation of radiometric contrasts is discussed for some simple models of terrain targets.

GLOSSARY OF SYMBOLS

Superscripts: primes denote "effective" quantities

Subscripts (generally, with exceptions as noted):

f = "spectral" quantity

b = background

i (or j) = incident radiance

r, t = reflected, transmitted

$0, 1$ = reference quantity (standard)

Particular symbols:

Page

a_1 = mean fractional absorption per unit raypath length

a', a'', a''' = mean fractional absorption ("absorptivity") for raypaths ℓ', ℓ'', ℓ'''

A', A'', A'''' = effective temperature of (medium containing) path length ℓ', ℓ'', ℓ'''

A_i, A_t = areas

B_O = postdetection bandwidth of radiometer

b = time constant for 5.4-db response of video output circuit of radiometer

B = predetection bandwidth

B = spectral radiance or brightness of a blackbody ($\text{W/m}^2 \text{ ster Hz}$)

B_i (or j), B_r, B_t = brightness of incident, reflected, and transmitted radiances

c = speed of light

e = emissivity (of target)

e_b = emissivity of background

e_f = spectral emissivity

e', e'', e'''' = mean fractional emission over raypaths $\ell', \ell'',$ and ℓ'''' , respectively

f = frequency (Hz)

F = beam-filling factor

G = spectral brightness of a greybody ($\text{W/m}^2 \text{ ster Hz}$)

h = Planck's constant

h = altitude

k = Boltzmann's constant

K, K_1 = radiometer detection constants

$\ell, \ell', \ell'', \ell'''$ = raypath lengths

L = loss factor = $1/t$

p = picture elements scanned per second

Q = radiometer generic constant

r = reflectivity

r_f = reflectivity (spectral)

r_b = reflectivity (background)

t = transmissivity

t_f, t_b = transmissivity, spectral and background, respectively

t', t'', t''' = fractional transmission for raypath lengths
 ℓ', ℓ'', ℓ'''

T = temperature of target

T_b = temperature of background

T_{bb} = temperature of blackbody

T_i, T_j = brightness temperature of the irradiation about to
 be reflected (i) or transmitted (j) by a target

T_s = sky temperature

T'_e, T'_r, T'_t = effective emissive, reflective, and transmissive
 temperatures

T_0, T_1, T_a = reference or normalization temperatures

T_A = apparent antenna temperature

T_{eff} = equivalent input noise temperature of receiver

x, y, z = Cartesian coordinates

$\alpha(x, y, z)$ = per unit length attenuation at point (x, y, z)

δT = sensitivity of radiometer

$\Delta T'$ = target-to-background contrast = $T' - T'_b$

$\Delta T''$ = background contrast at radiometer sensor, assuming target completely fills sensor antenna beam = $t' \Delta T'$

$\Delta T'''$ = apparent contrast (available at sensor input) = $F \Delta T''$

θ, ϕ, ψ = angles

τ = integration time constant of radiometer

Ω = solid angle (steradians)

1. INTRODUCTION

Real-time radiometric mapping of terrain with portable remote sensors has been proposed for airborne map-matching navigation. The real-time generated map is to be compared with a stored reference map of the desired route and measured differences between the maps can then be suitably interpreted as error signals for the navigation system. Feasible automation of these navigating techniques would make them attractive for C/VSTOL all-weather airbus service.

Radar mappers are active-mode systems, i.e., a radar transmitter and receiver are co-located (in an aircraft) and together scan a given field of view, leading to a two-dimensional display or image of the latter. Radiometric mappers, on the other hand, operate in the passive mode - the mapper contains a receiver but no transmitter - and produce images of the natural electromagnetic (thermal) emanations included in their field of view. When artificial, very bright sources are deliberately located in its field(s) of view; the radiometric mapper is said to operate in the augmented passive or else semiaactive mode.

Since microwaves are capable of penetrating the atmosphere with little loss or interference even in the worst weather, the use of these waves for all-weather navigation systems has been proposed. The short wavelengths of the mm band make possible small and light electronic hardware, as well as fine image-resolving capability. For short- or intermediate-haul distances (≤ 500 miles), passive radiometry at mm wavelengths may be a convenient mode of enroute navigation for airbus route traffic and general aviation aircraft. It may be economical on the basis that (1) the all-weather capability eliminates grounded-time

loss and (2) the ability exists to establish new traffic routes by the relatively simple expedient of generating a reference map by a single clear-weather (standard) overflight of the new terrain. In addition, there exists the potential for full automation of radiometric map-matching techniques. Furthermore, such systems, suitably enlarged in functional scope, may also supplement instrument landing systems or ground traffic control systems.

In Section 2 of this report, we review some elements of microwave radiometry, collect some radiometric data pertinent to the K_a -band regime (~ 35 GHz), and examine the radiometric contrast available as input to the antenna of an airborne radiometer-receiver, under various weather conditions. In Section 3, we present some results of radiometric contrast calculations for some simple targets.

It will be seen that the normal variations in terrain temperature and moisture content associated with diurnal and seasonal weather changes render unreliable the unaugmented radiometric contrast (terrain signature) available to the radiometer as signal input for purposes of purely passive mode navigation.

Map-matching techniques for radiometric navigation (correlation functions, error signal generation, contour enhancement, and electronic or optoelectronic data processing) will be presented in a separate report. The present one is concerned primarily with the characteristics of the signal fields the radiometer must sense, and secondarily with the sensitivity of the sensors required for radiometric navigational systems.

2.1. ELEMENTS AND NOTATIONS FOR MICROWAVE RADIOMETRY (1)*

Planck's law gives the spectral *radiance* or "brightness" of a blackbody (perfect radiator) at uniform temperature T_{bb} as

$$B(f, T_{bb}) = \frac{2h(f^3/c^2)}{[exp(hf/kT_{bb}) - 1]} \quad W/m^2 \text{ ster Hz} \quad (1)$$

Here f is frequency and c , h , and k are the speed of light and the constants of Planck and Boltzmann, respectively.** For $f \leq 300$ GHz, the above is approximated to within 3% by

$$B(f, T_{bb}) = \frac{2kf^2T_{bb}}{c^2} \quad (2)$$

which shows linear proportionality $B \sim T_{bb}$ (the Rayleigh-Jeans regime).

A greybody (imperfect radiator) is characterized by a radiative efficiency factor e_f , the emissivity. For such a body, at thermometric temperature T , emissivity is defined as the observed spectral *radiance* of the greybody $G(f, T)$ normalized to the radiance of a blackbody at the same temperature and wavelength:[†]

$$e_f = \frac{G(f, T)}{B(f, T)} , \quad (T_{bb} = T) \quad (3)$$

The greybody of interest - the "target" - may be said to have an *effective* or emissive target temperature T'_e defined by:[§]

*Numbers in parentheses refer to references listed in Section 5.

**MKS units will be used, except as noted.

[†]In this report (cf. discussion below Equation 7), all greybodies and targets of interest (except as noted) are assumed to have random, rough surfaces, i.e., to be diffuse rather than specular reflectors.

[§]Effective temperatures will be denoted by primes (single or multiple) throughout.

$$G(f, T) = B(f, T_{bb} \equiv T'_e)$$

Referring to Equation 3, we may then write

$$e_f = B(f, T'_e) / B(f, T)$$

or, using Equation 2:

$$e_f = T'_e / T .$$

Hence

$$T'_e = e_f T . \quad (4)$$

Target reflectivity is the ratio of the radiance of the reflected radiation to the radiance of the incident radiation (cf. Fig. 1)

$$r_f = B_r / B_i \quad (\text{omitting arguments } f \text{ and } T)$$

If incident and reflected radiations are assigned apparent temperatures T'_r and T_i via Equation 2, we can ascribe to the target an *effective* reflective temperature given by

$$T'_r = r_f T_i . \quad (5)$$

Similarly, for power transmitted through the target, transmissivity t_f , transmitted radiance B_t , incident radiance B_j , and effective transmissive target temperature T_t , are defined in the manner of Equation 2 by (cf. Fig. 1):

$$\left. \begin{aligned} t_f &\equiv B_t / B_j \\ T'_t &= t_f T_j \end{aligned} \right\} \quad (6)$$

Hence, for thermal steady-state equilibrium conditions, accounting for a possible multiplicity of radiation sources (e.g., B_i and B_j in Fig. 1),

the effective target temperature is

$$\begin{aligned} T' &= T'_e + T'_r + T'_t \\ &= e_f T + r_f T_i + t_f T_j . \end{aligned} \quad (7)$$

Subscript f , which stresses the frequency dependence of e , r , and t , will be dropped for simplicity. These coefficients have, in addition, complicated dependence on geometric and molecular constituent parameters of target surface and volume. For example, for the target of Figure 1, as seen by the indicated sensor:

$e = e (f, T; \text{ polarization; } \phi, \psi; \text{ surface roughness; dielectric and magnetic permeability; conductivity; subsoil moisture and composition, etc.})$

We will generally be concerned with random (rough-surface or "diffuse") reflectors rather than specular reflectors. Regarding composition, moisture content is particularly influential because of the high dielectric constant of water. In many situations, it suffices to determine an emissivity by operational or measurement techniques and then define an effective emissivity.

Most targets of interest will be opaque and satisfy:

$$r = 1 - e \quad (t = 0) \quad (8)$$

Equation 7 then simplifies to

$$T' = eT + rT_i = e(T - T_i) + T_i \quad (9)$$

Assuming the terrain adjacent to the target has some irradiation brightness ($B_i \sim T_i$, $B_j \sim T_j$), spectral parameters e_b , r_b , t_b , and thermometric temperature T_b , the apparent temperature of the background is

$$T'_b = e_b T_b + r_b T_i + t_b T_j \quad (10)$$

which is Equation 7 modified only by subscript b. For opaque background material ($t_b = 0$, $r_b = 1 - e_b$), the counterpart of Equation 9 is

$$T'_b = e_b T_b + r_b T_i . \quad (11)$$

Then at the target, or in the absence of any medium intervening between target and sensor, at the sensor there is a brightness contrast between target and background - "background contrast" - defined by*

$$\begin{aligned} \Delta T' &= T' - T'_b \\ &= eT - e_b T_b + (e_b - e) T_i . \end{aligned} \quad (12)$$

T_i in the last term represents the temperature of radiation reaching the target along line of sight ϕ_i, ψ_i (see Figure 1) and is the apparent temperature of the sky (in that direction) as seen by the target.**

As illustrated in Figures 1 and 2, the following terminology is adopted here. Target parameters bear no subscript; background parameters have subscript b. Parameters for target-to-sensor transmission path have a single prime; for target-to-exosphere path, double primes; for sensor-to-exosphere path, triple primes. Mean thermal temperatures are

*The microwave practice of calling this unnormalized difference a "contrast" differs from the photographic practice of designating as "contrast" only normalized parameter differences.

**Properly speaking, radiation from all parts of the sky is reflected in part along direction ϕ, ψ . Commonly (Ref. 3), product $r_b T_i$ is determined by Equation 11 and r_b is measured. Then T_i (computed) is assigned the direction $\phi_i \equiv \phi$, $\psi_i \equiv \pi - \psi$.

given by T , T_b , A' , A'' , A''' ; superscripts on T have meanings distinct from path designation.

If $e_b - e$ or T_i is small enough - a common enough occurrence - the last term in Equation 12 may be neglected and the simpler form,

$$\Delta T' \approx eT - e_b T_b \quad (12a)$$

is usable.

Let the exoatmospheric brightness temperature of the sky be T_s , and the target-to-exosphere pathlength be ℓ'' . In the absence of precipitation on ℓ'' , let the mean effective absorption temperature of the atmosphere be A'' (for path ℓ''), the fractional transmission through the atmosphere t'' (spectral), mean effective fractional atmospheric emission e'' , fractional reflection r'' , and fractional absorption a'' . If (as frequently) r'' is negligible, we have $e'' = 1 - t''$, and $a'' = e''$. The connection between T_s and T_i is then seen to be:

$$T_i = t'' T_s + e'' A'' = t'' T_s + a'' A'' . \quad (13)$$

The term $a'' A''$ consisting of effective temperature and absorption may be expressed in terms of the incremental, local (spectral) atmospheric absorption α , the local atmospheric temperature T_α , and the height of the atmosphere h'' :

$\alpha = \alpha(x,y) = \alpha(\ell) =$ per unit length attenuation at point x,y which is distant ℓ along direction ϕ ;

$T_\alpha = T_\alpha(x,y) = T_\alpha(\ell) =$ temperature at x,y .

The connection is given by (2-4):

$$e'' A'' = a'' A'' = \int_0^{h'' \sec \phi} \alpha T_\alpha \exp \left(- \int_0^{h'' \sec \phi} \alpha d\ell \right) d\ell \quad (14)$$

Frequently, in calculations of transmission through lossy electronic as well as terrestrial media, the transmission loss factor

$$L'' = 1/t'' \quad (15)$$

is commonly used to characterize (e.g.) particular portions of a radiometer input network.

The portion of the atmosphere between target and sensor (cf. Fig. 2) may likewise be characterized by (single-primed) counterparts: ℓ' , A' , a' , e' , r' , t' . Therefore, at the sensor the observable brightnesses, when viewing target and background, respectively, are

$$T'' = t'T' + e'A' + t'''T_s + e'''A''' \quad (16)$$

and

$$T_b'' = t'T_b' + e'A' + t'''T_s + e'''A''' . \quad (17)$$

The last two terms in the above represent brightness contribution due to the portion of atmosphere above the sensor (see triply primed symbols in Fig. 3).

With the aid of Equations 9 and 13, we may show the dependence of the sensed temperature field (T'') on the target and (mean) atmospheric temperatures (T , A' , A'' , A''') and parameters (e , . . . , t'''):

$$T'' = t'eT + t'rt''T_s + t're'''A'' + e'A' + t'''T_s + e'''A''' . \quad (18)$$

The peak contrast at the sensor is the briefer expression:

$$\Delta T'' = T' - T_b' = t'(T' - T_b) = t'\Delta T' . \quad (19)$$

A scanning sensor (antenna) alternately viewing target only and background only would indicate, respectively, T' and T_b' ; but while scanning

through borders between target and background it would sense compositely based temperatures intermediate in value to T' and T'_b .

The energy-collecting aperture of the sensor will be assumed (first) to be an *ideal* pencil-beam antenna, i.e., one having uniform gain over a sharply defined solid angle of reception*

$$\Omega_i \doteq \theta_i^2 \quad (20)$$

and vanishing gain outside this. The target subtends at the sensor the solid angle

$$\Omega_t = A_t \cos \phi / \ell^2 \quad (21)$$

where A_t is the portion of the target area (projected into the median ground plane of the pencil beam; see Fig. 3) that falls inside the ideal scanning beam. At distance ℓ , the cross-sectional area of this ideal beam is

$$A_i = \ell^2 \theta_i^2 = \ell^2 \Omega_i .$$

Hence, the fraction of the antenna beam occupied by the target, the beam-filling factor F , may be written:

$$F = \Omega_t / \Omega_i = A_t \cos \phi / A_i = A_t \cos \phi / \ell^2 \theta_i^2 \quad (22)$$

with $F \leq 1$ and equality holding for $\Omega_t \geq \Omega_i$. With $\Omega_t < \Omega_i$, the sensor sees background in the solid angle $\Omega_b = \Omega_i - \Omega_t$, and senses the weighted temperature or *apparent target temperature*:

$$T''' = FT'' + (1 - F)T'_b \quad (F \leq 1) . \quad (23)$$

*An equally common notational practice replaces θ_i here by $\theta_i / \sqrt{4\pi}$.

The corresponding *apparent* contrast is therefore

$$\Delta T''' = T''' - T_b''' = F\Delta T'' = Ft'\Delta T' \quad (24)$$

which is explicitly:

$$\Delta T''' = Ft'[eT - e_b T_b + (e_b - e)T_i] \quad (25)$$

$$= Ft'[eT - e_b T_b + (e_b - e)(t''T_s + e''A'')] . \quad (26)$$

This important result is seen to be a complex function of frequency, polarization, target-background-sensor geometry, physical constitutive parameters, antenna pattern (implicit in F), etc. Some of these will be briefly discussed (next section). Before doing so, we note a simplification of Equations 13 and 25. Because the exoatmospheric sky temperature T_s is only of the order of $3-4^\circ$ (while $t'' \leq 1$), we may usually neglect $t''T_s$ compared to $e''A''$, even if $t'' > e''$; hence

$$T_i \approx e''A'' = (1 - t'')A'' = a''A'' . \quad (27)$$

Then Equation 26 simplifies somewhat to

$$\Delta T''' = Ft'[eT - e_b T_b + (e_b - e)e''A''] , \quad (28)$$

the *apparent* contrast at the sensor antenna input.

If the radiometric behavior of the atmosphere were ideally transparent for target sensing, we would have $t' = 1 = t''$ (and $e' = 0 = e''$), in which case the "ideal" apparent contrast would be

$$\Delta T''' = F(eT - e_b T_b) . \quad (29)$$

For such "ideal" atmospheric transparency, Equation 18 becomes simply

$$T'' = eT + rT_i = eT + (1 - e)T_i \quad (30)$$

2.2. RADIOMETRIC PROPERTIES OF TERRAIN AND ATMOSPHERE

In this section we collect some data on emissivity, transmissivity, temperature, and other characteristics of atmosphere and terrain under a variety of conditions - seasonal, daily, etc. - for frequencies neighboring 35 GHz. Figure 4 shows apparent sky temperature (T_i in Equations 12 and 13) measured at mm wavelengths by Wulfsberg (2) who found that:

$$T_i(\phi) = (1 - t_o^{\sec \phi}) T_m \quad (31)$$

where

t_o = fractional transmission of the atmosphere at zenith (cf. t' in Fig. 2)

ϕ = zenith angle

$T_m = 1.12T_g - 50$

T_g = surface temperature of the ground (in °K)

T_m was found to be essentially independent of frequency (in this regime).

Measurements at 35 GHz and at frequencies down to 10 GHz are well fitted by Equation 31.

Figure 5, also from Ref. 2, is a reminder of the influence of antenna reception pattern on the indicated radiometric temperature.

Figure 6 shows one-way attenuation ($a' = 1 - t'$ for specified ray pathlength ℓ' , as in Fig. 2), expressed in decibels, in convenient parametric form, for various weather conditions (4).

Figure 7 shows theoretical curves of one-way specific attenuation (a , db/km) for microwaves and mm waves computed by Broussard and Richard (5) which serve (in a more general way than Fig. 5 does) as rough and ready tools in the absence of precisely known data.

Figure 8 shows a frequency panoramic view of molecular effects in atmospheric absorption according to Meyer (6).

Figure 9 shows University of Texas data (3) on the apparent temperature of asphalt viewed from various directions at ground level, for various weather (sky temperature) conditions. The emissivity of the asphalt is Lambertian: $e = 0.9 \cos \phi$, and its thermal temperature is 290° K. Test frequency was 70 GHz (4.3 mm wavelength) and polarization horizontal.

Figure 10 shows for convenience (4) a plot of the frequently used relations of Equations 8 and 9.

Before proceeding to review the emissivities of materials of interest, it is worth noting the typical gross range of variation of the thermometric (thermodynamic) temperature of sample terrain. Figure 11 shows typical daily variations for a variety of weather conditions: clear or cloudy, dawn or dusk, and (for mountain and valley) day or night (7). For sand beach the difference shown here between typical clear day and cloudy day Kelvin temperatures is $318^\circ - 285^\circ = 33^\circ$; such a beach, having emissivity 0.8, has effective radiometric temperatures of 309° (day) and 282.6° (night), and the radiometric difference of 26.4° . For bodies having low emissivity (e.g., metals), effective emissivity temperatures tend to be low; hence their illumination by nearby warm objects tends to determine their effective, mostly reflective, temperatures.

Since emissivity is a complex function of numerous material properties (dielectric and permeability "constants", surface roughness, subsurface composition, surface orientation) and numerous radiation field properties (frequency, polarization, propagation direction) measured emissivity data may be said to be as reliable as the extent to which measurement conditions are specified in detail. Because of the complexities of specifying emissivity, one common practice is to display the

"raw data" (apparent temperature) of the material under test, as illustrated in Figures 13 to 19.

Figure 12 shows calculated reflectivity (r) and *surface emissivity* ($1 - r$), for an "infinitely" large body of smooth water, as function of polarization and grazing angle (8). The indicated frequency is 24.2 GHz.

Figure 13 shows *effective emissivity* for soil of varying surface roughness ("specular" and "diffuse"), as well as varying moisture content and depth, as a function of angle of incidence (9). These data are for horizontally polarized receiver operated at 16.7 GHz. The more common mode of data display is shown in Figure 14 where apparent or brightness temperature of the test material, $T' = eT$, is plotted for grass, concrete, water, and a metal plate for varying incidence and polarization at 19.4 GHz.*

Figure 14 suggests, according to Pascalar (10), that observations at 45° incidence and both polarizations provide a unique method of identifying the presence of small water bodies.

Figure 15 illustrates typical emissivities of various materials at normal viewing at K_u and K_a band frequencies (11).

In Figures 16-19 are collected some additional K_a -band data of interest. The surprising suggestion appears in Figure 16 that wet snow has approximately unity emissivity (12). In Figure 17 the low emissivity of mud, perhaps ascribable to its water content, is noteworthy; Figure 18 shows polarization dependence of some terrain materials; Figure 19 compares emissivities of fresh and salt water at X- and K_a bands (13). Figure 19 illustrates again the influence and contribution of sky temperature and weather conditions in determining the apparent temperature of a target (3).

*The term T in the above may be assumed to be 290° K for most materials plotted, and the characteristic 273° K for ice.

2.3. RADIOMETRIC CONTRAST AS FUNCTION OF TARGET, BACKGROUND, AND SENSOR GEOMETRY

We recall Equation 28 in the form

$$\begin{aligned}\Delta T''' &= Ft' [eT - e_b T_b + (e_b - e) T_i] \\ &= \text{fill factor} \times \text{transmission factor} \times \text{background contrast}\end{aligned}\quad (32)$$

The radiometric contrast at the antenna input is atmosphere-dependent through T_i (cf. Eq. 7 or 31) and t' (which is obtainable from Fig. 8 or 7), for given target-to-sensor, slant range. For the data of Figure 8, the transmittance t' may be represented approximately by

$$t' = \exp(-0.23a_1 l) . \quad (33)$$

where a_1 is the specific logarithmic absorption coefficient (absorption in decibels per unit length), a function of altitude. Here slant length l is related to sensor altitude h (see Fig. 4) by

$$l = h \sec \phi . \quad (34)$$

By means of Equations 33, 34, and 22, Equation 32 for radiometric contrast may be rewritten:

$$\begin{aligned}\Delta T''' &= \underbrace{\frac{A_t \cos \phi}{\theta_i^2 (h \sec \phi)^2 \exp 0.23a_1 h \sec \phi}}_{\text{contrast coefficient}} \underbrace{[eT - e_b T_b + (e_b - e) T_i]}_{\text{background contrast (Eq. 12)}} \\ &= \text{contrast coefficient} \times \text{background contrast (Eq. 12)}\end{aligned}\quad (35)$$

This expression for radiometric contrast allows for characteristics of the target (A_t, ϕ, e, T), of the background or ambient (e_b, T_b, T_i, a_1, ϕ), and of the sensor geometry (h, ϕ, θ_i). The role of sensor electronics is discussed in the next section.

Since $\phi \leq 90^\circ$, the coefficient of the bracketed factor is intrinsically positive. Depending on whether $T'' \geq T_b''$, accordingly $T''' \geq 0$ (cf. Eq. 24). Since detectability of a target depends not on sign but magnitude, we will plot only $|\Delta T'''|$ as is the practice. As will be seen, $|\Delta T'''| \sim 1^\circ\text{-}5^\circ \text{ K}$ for practical targets of interest under a variety of realistic circumstances; hence power detectors of considerable temperature sensitivity must back up the sensor antenna.

2.4. RADIOMETER AND SCANNING CONSIDERATIONS (14)

Behind the antenna, which senses the broadband random thermal noise power characterized by T'' or T''' , is a receiver - a power detector - that measures the apparent temperature of the antenna to which it is connected. The sensitivity (minimum detectable temperature change) of a radiometer system is given by

$$\delta T = QF_o T_o (b/B)^{1/2} \quad (36)$$

where F_o = noise figure, T_o = reference temperature (290° K), b = post-detection filter bandwidth between 5.4-db amplitude response points (defined by $b = 1/4RC$), B = predetection bandwidth, and Q = radiometer generic constant ($Q = 2$ for a dc radiometer; $Q = 2\sqrt{2}$ for a square wave switched Dicke radiometer). δT represents the smallest change (rms value) in the amount of incident power ($\Delta P = k\delta T\Delta f$) that the radiometer can reliably detect, corresponding to unity signal-to-noise ratio.

Commonly used alternate forms of Equation 36 are

$$T = \frac{T_A + (F_o - 1)T_a}{(KB/B_o)^{1/2}} = K \frac{T_A + T_{eff}}{(B)^{1/2}} \quad (36a)$$

where B_O = output signal (postdetection) noise bandwidth; K, K_1 = detection constants, dependent on receiver configuration; T_a = noise figure normalization temperature ($= 290^\circ \text{ K} = T_O$ of Eq. 36); T_A = apparent antenna temperature; $T_{\text{eff}} = (F_O - 1)T_a$ = equivalent input noise temperature of the receiver; $\tau = RC$ = integration time constant of postdetection electronics (assumed to be an RC network). Comparison of different radiometers is usually based on the numerical value of the figure of merit

$$C = \delta T(\tau)^{1/2} = K_1 T_O F_O / B_O^{1/2}$$

evaluated for $\tau = 1$ sec of integration time.

Figure 20 indicates (1970) state of the art, showing this index plotted for various reported radiometric receivers (1). Typical of radiometer art (if not of reportorial art) for the mm-wave regime is the receiver described by Jordan and Pascalar (15). This is a Dicke-type square-wave-modulated, heterodyne-principle solid-state receiver. A specially developed balanced mixer* is integrally structured with a broadband UHF low-noise transistor IF preamplifier; the IF bandwidth permits double sideband operation. Operating frequency is 35 GHz. Pre-detection bandwidth (effective) is 600 MHz. Double sideband overall noise figure is 10 db. For an integration time of 1 sec, the rms value of temperature fluctuation δT was found to be 0.2° K , in close agreement with Equations 36, which yield 0.17° K . If F_O were 7 db rather than 10 db, other parameters unchanged, the instrument sensitivity would be doubled ($\delta T \approx 0.085^\circ \text{ K}$); if instead τ were limited to 10 msec (a 100-fold change) with other parameters unchanged, sensitivity per Equation 36 would be reduced (10-fold) to $\delta T \approx 1.7^\circ \text{ K}$. At 35 GHz, typical

*Details (proprietary) withheld.

good radiometers have $\delta T \sim 0.1 - 1^\circ K$. For fuller discussion of radiometer instrument electronics, the reader is referred to references cited in (14).

For radiometric map-making (imaging), the target area is scanned in two dimensions through peak-to-peak fore-aft and lateral scan angles of amounts $2\Phi_f$ and $2\Phi_l$, respectively, as illustrated in Figure 3. The map consists of a mosaic of picture elements, the latter being the beam cross section projected into the target (horizontal) plane. This area, $A_i \sec \phi$, determines the spatial resolution of the target (or "of the map"). The temperature resolution of each picture element, on the other hand, depends on the integration time devoted to its measurement. If p is the number of picture elements scanned per second, the minimum postdetection bandwidth required for adequate spatial resolution is $b' \approx p/2$, where b' is the 3-db bandwidth of the filter and is related to b (the 5.4-db point represented in Equation 36) by $b' = 2b/\pi$. Combining these two results, we have

$$p \approx 4b/\pi \quad (\text{picture elements/sec}) . \quad (37)$$

Hence Equation 36 may be expressed as

$$\delta T = Q_p F_o T_o (p/B)^{1/2} \quad (38)$$

where

$$Q_p = (\pi)^{1/2} Q/2 . \quad (39)$$

Assuming that the scanning pattern is as shown in Figure 21, where the fore-aft scan component is provided by the ground velocity of the airborne sensor, the scan rate becomes

$$p = 2\Phi_l V_g \cos^2 \phi / \theta_i^2 h \quad (40)$$

and the radiometer sensitivity is expressible as

$$\delta T = (Q_p F_o T_o \cos \phi / \theta_i) (2\phi_l V_g / Bh)^{1/2} \quad (41)$$

for which the dependence on the operational velocity-height ratio is noted in Figure 22.

A target is "detectable" if $\Delta T''' \geq \delta T$, and for best system performance one optimizes (usually maximizes) the contrast-to-sensitivity ratio (cf. Eqs. 35 and 41):

$$M = \frac{\Delta T'''}{\delta T} = \left(\frac{Bh}{Q_p F_o T_o} \right)^{1/2} \frac{A_t [eT - e_b T_b + (e_b - e) T_i]}{\theta_i (h \sec \phi)^2 \exp 0.23 a_1 h \sec \phi} \quad (42)$$

We see here the sensitive dependence of M on sensor altitude ($M \sim 1/h^{3/2} \exp Kh$), a parameter that might well be the focus of initial rather than final consideration in airborne navigation systems design. For other quantities constant (notably a_1), M decreases with increasing h . For vertical viewing ($\phi = 0$) and other variables again constant M is maximized with respect to ϕ . Larger targets (A_t) are more readily detected with narrower pencil beams (θ_i), as correspondingly larger M values result.

3. SOME BACKGROUND CONTRAST CALCULATIONS

The background contrast $\Delta T'$ represented by the bracketed factor in Equation 42 (cf. also Eq. 12 or 35) is uniquely characteristic of the target area. We may rewrite it in the manner of Hooper and Battles (16):

$$\Delta T' = eT - eT_1 \quad (43)$$

where T_1 is the reference temperature

$$T_1 = (T_b - T_i)e_b/e + T_i . \quad (44)$$

T_1 is dependent on four parameters relating to target (e), background (T_b , e_b) and "sky" (T_i); it is shown plotted in Figure 23 as a function of e_b/e . The background contrast, which depends on the fifth parameter T as well, may then be expressed in terms of the normalizing or effective reference temperature eT_1 as

$$\frac{|\Delta T'|}{eT_1} = \left| \frac{T}{T_1} - 1 \right| \quad (45)$$

which is plotted in Figure 24.

Detectability of a target can be critically small for the condition

$$\Delta T' = e(T - T_i) - e_b(T_b - T_i) \approx 0 \quad (46)$$

which is alternately expressible as

$$|\Delta T'| < eT_1 \quad \text{or} \quad |T' - T_1| < T_1 . \quad (47)$$

From the equivalent of Equation (46)

$$e(T - T_i) \approx e_b(T_b - T_i) \quad (46a)$$

we see that for given background conditions (e_b , T_b , T_i) the above conditions are satisfied, i.e., a given target may have low detectability - with the target parameters (e , T) suitably satisfying any one of three conditions: (1) for $e > e_b$, $T < T_b$, (2) for $e \approx e_b$, $T \approx T_b$, and (3) for $e < e_b$, $T > T_b$. These represent somewhat different physical conditions.

To illustrate the use of the foregoing, suppose we are told $e_b/e = 1.5$ and are given $T = T_a$. In Figure 23, T is plotted as ordinate on the right. Starting from the point $(e_b/e, T) = 2.0, T_a$ we may

trace to the specified coordinate $(1.5, T_a)$, thence to the intersection of the T_1 -line (the main indicated "diagonal") with the ordinate line (vertical) at abscissa $e_b/e = 1.5$. This intersection at $(e_b/e, T_1) = (1.5, T_c)$ determines the function $T_1 = T_1(e_b/e, T)$. The scale of the figure is set by T_b and T_i , which are generally known or prescribed. For points $(e_b/e, T)$ on the T_1 -line $\Delta T' = 0$, while for points near this line, the radiometric contrast is low. Figure 24 shows normalized brightness plotted against normalized target temperature in the all important neighborhood of vanishing radiometric contrast.

Figure 25 shows $\Delta T'''$ as a function of h for various targets ($0.88 \leq e \leq 0.91$; $T = 300^\circ$ or 325° ; $A_t = \text{fixed} = 500 \text{ ft}^2$) viewed normally on a clear day in a fixed background ($e_b = 0.97$, $T_b = 300^\circ$) with an X-band antenna of 1° beamwidth. Since only target parameters e and T are varied, only the brightness contrast $\Delta T'$ is directly altered and $\Delta T'''$ changes in proportion to this. For $T = T_b = 300^\circ$, with increasing emissivity the curves intersect the reference line $\Delta T''' = 1^\circ$ at successively lower altitude, until $e = e_b = 0.97$ is reached, in which case $\Delta T' = 0 = \Delta T'''$ (cf. Eq. 12) independently of altitude (and the "curve" is represented by the abscissa axis). For the targets having thermometric contrast $\Delta T = T - T_b = 325^\circ - 300^\circ = 25^\circ \text{ K}$ and with Equation 12a applicable, the brightness contrast and radiometric contrast vanish for

$$e \approx e_b T_b / T = 0.97 \times 300/325 = 0.896 .$$

The sensitivity of $\Delta T'''$ to variation in target temperature is notable from curves I and II of Figure 25: here the two targets having $e = 0.88$ differ in thermometric temperature by only $\Delta T = 25^\circ$ but their heights for unity contrast temperature differ by $\Delta h \approx 3300-1300 \approx 2000 \text{ ft}$ ($\Delta h/h_{\text{mean}} \sim 20/23 \sim 85\%$).

3.1. Radiometric contrast ($\Delta T'''$) and unity-contrast height (H_1) for some simple targets.- In this section we present some results of target contrast calculations for various targets and weather conditions for targets having fixed aspect but varying sensor antenna beamfill.

The variation in beamfill may arise from a change in the range from a fixed target to a receding sensor whose viewing aspect (orientation) does not change; in this case height must change in proportion to range change. Figure 26 shows that if the intersection of two long roads crossing at right angles is viewed at fixed incidence angle, then with increasing range (r), the road (target) area included within the expanding footprint of the antenna beam is a varying quantity. It has been shown (16) that provided $X \ll 2b$ and $Y \ll 2a$ in this figure, the beamfill is to close approximation:

$$F = \frac{A_t}{A_i} = \frac{2aX + 2bY - XY}{\pi ab} \quad (48)$$

where

a, b = respectively, semimajor and semiminor footprint axes of the pencil beam

X, Y = widths of roads running, respectively, parallel to y and x axes

Using $r = h \sec \phi$, $2a = r \theta_y \sec \phi$, $2b = r \theta_x \sec \phi$, we may write Equation 48 as

$$F = \frac{4(Xh\theta_y \sec^2 \phi + Yh\theta_x \sec \phi - XY)}{\pi \theta_x \theta_y h^2 \sec^3 \phi} \quad (49)$$

For large height h , XY is negligible against the other terms in parentheses and to within a few percent accuracy,

$$F \approx \frac{4(X\theta_y \sec \phi + Y\theta_x)}{\pi \theta_x \theta_y h \sec^2 \phi} \quad (50)$$

If further $\theta_x = \theta_y = \theta_i$ then Equation 50 becomes

$$F \approx \frac{4(X \sec \phi + Y)}{\pi \theta_i h \sec^2 \phi} \quad (51)$$

For the case of a single straight road or river stretching along the flight path, the y axis in Figure 26, we have $Y = 0$ and Equation 49 becomes

$$F = \frac{4X}{\pi \theta_x h \sec \phi} \quad (52)$$

while for the case of a single road or river transverse to flight path:

$$F = \frac{4Y}{\pi \theta_y h \sec^2 \phi} \quad (53)$$

It should be noted that the above expressions apply when the strips of width X and/or Y are centered (rather than offset) within the elliptical footprint.

Hence for strip-geometry targets we obtain a radiometric contrast (from Eqs. 24, 50, 52):

$$\Delta T''' \approx \frac{4(X\theta_y \sec \phi + Y\theta_x) t' \Delta T'}{\pi \theta_x \theta_y h \sec^2 \phi} \quad \text{for intersection of roads} \quad (54)$$

$$\Delta T''' \approx \frac{4Xt' \Delta T'}{\pi \theta_x h \sec \phi} \quad \text{for transverse river or road } (Y = 0) \quad (55)$$

Formulas 48 to 55 express the fixed peak contrast observed for a stated symmetric target (of fixed temperature and emissivity occupying the center of a field of view in a symmetrically disposed background, also of uniform temperature and emissivity). For the case that the sensing beam scans transversely through a target whose dimension along the

scan direction is finite, the variation of radiometric contrast with scanning motion may be a characteristic (a signature) identifying the terrain and may be useful for navigational purposes. Simple examples of radiometric contrast as a function of scan through target are illustrated in Appendix I. These illustrate the onerous algebra resulting from the complex analytical beamfill expression for even simple target geometries.

Figures 27 and 28 illustrate results of calculation with Equation 55 for selected cases whose descriptive data are in Table I.

For Figure 27 the target is a straight concrete road lying along the flight path and bordered by grass. The road is 20 ft wide, has emissivity 0.8, and is viewed with a 1° wide sensor beam at 45° target aspect. For two different weather conditions, the radiometric contrast is plotted as a function of altitude, and represented as curves A and B; the corresponding (calculated) background contrasts are listed in Table I. The high altitudes at which the road is detectable is worth noting: the abscissa is in kilofeet. This would appear to be quite adequate for short-haul or intermediate-haul contemplated enroute altitudes of ~2-5 kilofeet. Curve C in the same figure shows the substantially larger contrasts available when observing a road 60 ft wide with a sensor beamwidth of 0.5° . Since $\Delta T''' \sim F \sim X/\theta_x$ (cf. Eqs. 52 and 55), it is clear from parameter values noted that the ordinates of curve C are six times those of curve A.

The weather- and moisture-dependent nature of the terrestrial surface itself, as noted from Figures 13, 17, 18, and 24, emphasize the possibility of having underlying terrain move from a usable radiometric contrast of say 10° into the zero contrast regime in virtue of some rainfall, snowfall, or other mode of collecting moisture (e.g., due to the road being part of a

valley or drainage basin), or the contrary possibility of having terrain, which was marked at zero contrast (i.e., akin to background) on the reference map, suddenly crop up as a target of high (say 10°) contrast. Rain effects on targets (and backgrounds) may conceivably alter emissivities of materials in the field of view.* Changes in emissivity of target and/or background generally alter the background contrast, $\Delta T'$, hence the observable, $\Delta T'''$. Curve D in Figure 27 results for a hypothetical lowering of emissivities, below the values listed for curves A to C, by arbitrary but nontrivial amounts ascribed to prior rainfall. (The thermal temperatures of materials in wet state have been assumed unchanged from the dry state, however.) Ordinates for curve D are here $\Delta T'_{\text{wet}} / \Delta T' \approx (-)51 / (-)27 \approx 1.89$ times the ordinates for curve C.

Figure 28 shows that a 200-ft-wide river furnishes high contrasts even at low altitudes. The enlarged abscissa scale should be noted. However, despite the indicated available contrasts of tens of degrees (even at 50 kft altitudes), the mapping or tracing of a river is still subject to some uncertainties of target (border) identification.

4. SUMMARY AND CONCLUSIONS

From the radiometric environmental data of Section 2 and the radiometric contrast calculations of Section 3, it can be seen that temperature contrasts ($\Delta T'''$) usable for navigational guidance are often obtainable from commonplace, simple geometric targets (e.g., roads, rivers, railways, well-defined crop fields, etc.).

*Battles and Hooper (16) consider only the effect rain has in lowering the thermal temperature of a target (e.g., by evaporation).

A fixed portion of terrain, or fixed field of view, may be imaged at a fixed (airborne) sensing location, and a "thermal map" of the terrain's temperature distribution may be constructed as a two-dimensional plot of isotherms (proportional to T''') or as some equivalent informational record. For fixed field of view and observation point, thermal maps taken on different days differ due to diurnal or seasonal variations of target temperature and/or emissivity. The sensed radiometric temperatures recorded as isotherms differ in geometric form and thus define different "thermal" boundaries for a given "optical" scene. It is these daily and/or seasonal variations ($\sim 10^\circ$ to 100° K at mm-wave radiometry) in the apparent borders of optically identifiable terrain targets which limit the reliability and accuracy of navigating by radiometric map-matching (see Figs. 11, 25, and 26). Even if technological limitations on sensor sensitivity (receiver noise figure) did not exist, the above variations would limit the attractiveness of radiometric navigation systems that do not employ man and his pattern-recognizing capability as key parts of the navigational decision process.

Where the dependence of radiometric temperature on seasonal and diurnal weather (and other) factors is well enough known, i.e., where extensive geological, meteorological, etc., data exist, it may be possible to employ one or a limited few reference maps for successful enroute navigation by optoelectronically automated, map-matching techniques. And by correlating an entire frame or field of view with its reference frame counterparts - rather than individual identifying objects or targets within the currently observed and the reference frames - improved (more reliable) error signals may be obtainable for guidance

purposes. The added cost or complexity of processing all the signal information in the field of view rather than the more limited information stored in a subportion of the field is not beyond current technology.

These same factors of seasonal and daily variations and fluctuations of observable radiometric temperature may seriously limit the utility of map-matching for the inexpensive establishment of new flight routes. For the initial overflight to yield a useful reference map for subsequent matching purposes, the statistics of T''' for the area overflown must be known well enough for confidence in using map-matching for a second (guided or controlled) overflight. Just what constitutes "well enough" has yet to be determined. (But whatever the added amount of information needed - and however minimal - it must produce a guidance system having comparable or greater navigational accuracy than is provided by current "area navigation" systems that compete for short- and intermediate-haul navigational service. The "area-nav" systems operating in the UHF and VHF bands have all-weather service capability and the navigational accuracy of ~1.0 nautical mile error in 400 nautical mile haul.)

Fundamental aspects of navigational radiometric map-matching and autocorrelation techniques will be examined in a companion report. Theory and experimental results for unclassified systems will be reviewed.

ACKNOWLEDGMENT

This manuscript has benefited much from critical reading and helpful comment by B. Ragent and J. Dimeff of the Instrumentation Division, NASA, Ames Research Center.

5. REFERENCES

1. Committee on Remote Sensing for Agricultural Purposes, Agricultural Board, National Research Council, *Remote Sensing* (National Academy of Sciences, PP&O, Washington, D.C., 1970).
2. Wulfsberg, K. N., Physical Sciences Research Paper 38 (AFCRL-64-590), A. F. Cambridge Research Laboratories, Microwave Laboratory, Hanscom Field, Mass., 1964.
3. Porter, R. A., in *Applications of Passive Microwave Technology to Satellite Meteorology: A Symposium* (Katz, Y., Ed.), Rand Corp. Memorandum R.M.-3401-NASA.
4. Lockheed Missile and Space Company, Rept. 5-26-68-1 (1968).
5. Broussard & Richard, in *Light and Heat Sensing*, 43-73 (Merrill, H. J., Ed., Pergamon Press, 1963).
6. Meyer, J. W., *Proc. IEEE*, 54, 484-492 (1966).
7. Conway, W. H., et al., *Proc. 2nd Symp. Remote Sensing of Environment*, Rept. 4864-3X, Univ. of Michigan, Inst. Sci. & Technol., 1963.
8. Lewis, E. A., et al., Electronics Research Directorate, AFRLDC, AF Cambridge Research Center, Tech. Rept. 54-G (1954).
9. Edgerton, et al., Aerojet-General Corp. Tech. Rept. 4, SGD 829-6, Contract NO nr 4767(00), NR 387-033 (1968).
10. Pascalar, H., *Proc. 14th Annual Technical Symposium of the Society of Photo-Optical Instrumentation Engineers* (San Francisco, Sacramento, 1969).
11. Kennedy & Jarga, in *I. R. S. I. Symposium on Remote Sensing* (Sacramento), 1, 183 (1969).

12. Edgerton & Trexler, *Proc. 6th International Symposium on Remote Sensing of Environment* (Univ. of Michigan), II, 767 (1969).
13. *Introduction to Electromagnetic Remote Sensing*, AGI Short Course Lecture Notes, American Geophysical Institute, Washington, D. C., pp. 3-5 (1968).
14. McGillem & Seling, *IEEE Trans. on Mil. Electronics*, MIL-7:(4), 296-303 (1963).
15. Jordan & Pascalar, *Proc. IEEE*, 53(10), 1655-1656 (1965).
16. Hooper & Battles, Naval Ordnance Laboratory, Corona, California, NAVWEPS Rept. 8140 (1963).

APPENDIX I. RADIOMETRIC CONTRAST AS FUNCTION OF SCAN THROUGH SIMPLE TARGETS

A1. Half-space target, one-dimensional scan, circular ideal pencil beam. - Let the ground plane consist of the infinite half-plane target $x > 0$ (shaded in Figure A1) at effective temperature T' ; and let the background be the half-plane $x < 0$ at effective temperature T'_b . Let the ideal sensing beam scan (at normal incidence) along the x axis; let the beam footprint be circular, of diameter D . Then the radiometric contrast may be expressed as a function of the amount of beam-target overlap (x), beam diameter (D), and the maximum radiometric contrast available:^{*}

$$\Delta T'_m = T' - T'_b = \text{maximum possible contrast} . \quad (\text{A1})$$

Basically, a beamfill factor is calculated. The target area within the sensor beam is

$$\begin{aligned} A(x) &= D^2\theta/4 - y(D/2 - x) \\ &= (D^2/4)[\cos^{-1}(1-2x/D) - 2(1-2x/D)\sqrt{(1-x/D)x/D}] \end{aligned} \quad (\text{A2})$$

The beam factor, as in Equation 22, is

$$F(x) = \Omega_t(x)/\Omega_i = A(x)/A(x=D)$$

$$F(x) = (1/\pi)[\cos^{-1}(1-2x/D) - 2(1-2x/D)\sqrt{(1-x/D)x/D}] \quad (\text{A3})$$

* $\Delta T'_m$ as given here is identical with the $\Delta T'$ defined in the text as Equation 12; the subscript m is here added merely to distinguish it from the variable $\Delta T'(x)$.

The effective contrast as function of beamfill is

$$\begin{aligned}\Delta T'(x) &= \Delta T'_m F(x) = \Delta T'(x/D) \\ &= \frac{T' - T'_b}{\pi} [\cos^{-1}(1-2x/D) - 2(1-2x/D)\sqrt{(1-x/D)x/D}] \quad (A4)\end{aligned}$$

For an assumed target and background difference of $\Delta T'_m = 5^\circ$ the radiometric contrast as function of normalized overlap is plotted in Figure A1.

The above may be put on a time basis for some given $x = x(t)$, e.g., if $x = Vt$ with V = velocity of sensor in the x direction.

A2. Rectangular target; rectangular ideal pencil beam. - Assume, as illustrated in Figure A2, a rectangular terrestrial footprint of dimensions $2A \times 2B$ form a normally incident ideal beam. Let the target be also rectangular of dimension $2a \times 2b$ with sides parallel to the footprint. Again let target and background effective temperatures be T' and T'_b with $T' - T'_b \equiv \Delta T'_m$, then

$A(x,y) =$ target area within sensor beam

$$= \begin{cases} 0, & \text{if } |x| > A+a \text{ or } |y| > B+b \\ (A+a-x)(B+b-y), & \text{if } |x| \leq A+a \text{ and } |y| < B+b \end{cases} \quad (A5)$$

$$= (A+a)(B+b) - (B+b)x - (A+a)y + xy \quad (A6)$$

and the fill factor becomes:

$$F(x,y) = \Omega_t(x,y)/\Omega_i = A(x,y)/4AB \quad (A7)$$

The resulting radiometric contrast is

$$\Delta T'(x,y) = \frac{\Delta T' F(x,y)}{m}$$

$$= \frac{T' - T'}{4} \left[\left(1 + \frac{a}{A} \right) \left(1 + \frac{b}{B} \right) - \left(1 + \frac{b}{B} \right) \frac{x}{A} - \left(1 + \frac{a}{A} \right) \frac{y}{B} + \frac{xy}{AB} \right] \quad (A8)$$

which is subject to conditions defined in Equation A5. So long as edges 2a and 2A are kept parallel to a fixed x-axis, radiometric contrast may readily be expressed as function relative scanning motion of target and sensor beam. For example, with $x = x(s)$, $y = y(s)$ given functions of s , $\Delta T'(xy) = \Delta T'(s)$ may be computed; the case of common interest is where s stands for time.

TABLE I. DATA FOR FIGURES 27 AND 28.
(Frequency band K_a (35 GHz); look angle $\phi = 45^\circ$)

Quantity	Symbols & Units	Curve A	Curve B	Curve C	Curve D	Remarks
Concrete road width	X ft	20	20	60	60	Fig. 27
River width	X ft	200	200	200	200	Fig. 28
Antenna beamwidth	θ_x deg	1	1	0.5	0.5	Sidelobes neglected; antenna efficiency, 55%; θ_x = half-pwr BW
Emissivity (ϵ at ϕ)	ϵ_e	0.8	0.8	0.8	0.7	Emissivities assumed independent of thermal temperature
Concrete	ϵ_b	0.97	0.97	0.97	0.95	
Grass	ϵ_e	0.34	0.34	0.34	0.34	
Water						
Weather conditions	Clear sky*	MR & MC**	Clear sky	Clear sky	Moisture content given, per Fig. 7a of Ref. 5, and curves f and c in Fig. 7, in footnotes below	
Attenuation	a_1 db/km	0.055	0.92	0.055	0.055	
Temperatures	T_i °K	25	104	25	25	
Apparent sky	T_i					
Sky seen upward	$T_i, 35$	0	0	0	0	
at 35 kft						
Concrete	T_o	325	290	325	325	Temperatures are illustrative
Grass	T_o	300	290	300	300	
Water	T_o	290	290	290	290	
Contrast	$\Delta T'$	(-)27 (-)76	(-)31 (-)16	(-)27 (-)76	(-)51 (-)76	
Concrete road						
River	H_1 kft	26 1190	24 875	133 (1297)	172 (1336)	$H_1 = h$ (for $\Delta T' = 1$) Fig. 27 Fig. 28, only curves A and B shown
Unity-contrast height						
Concrete (vs. grass)						
River (vs. grass)						

*Clear sky denotes 1% absolute H₂O vapor at sea level in dry air.

**MR & MC denote moderate rain and superposed moderate clouds. MR denotes uniform precipitation of 4 mm/hr from sea level (0 ft) to 3 kft. MC denotes uniform condensed H₂O content of 0.3 g/m³ from 3 to 6 kft altitude (visibility in cloud ~ 400 ft), superposed on clear sky model.

FIGURE CAPTIONS

Fig. 1. Target (e , r , t , T) and sensor terminology; n is normal to the median target surface; angles ϕ and ψ define target-to-sensor direction; ϕ_i and ψ_i define a target to exosphere direction.

Fig. 2. Sensor-target-sky configuration.

Fig. 3. Ideal pencil beam antenna and median ground plane traces (beam at center of scanning pattern).

Fig. 4. Sky temperature profiles at 35 GHz measured under various weather conditions.

Fig. 5. Composite of sky temperatures and antenna patterns. Antenna 3-db beamwidth: 3° at 35 Gc, 6° at 15 Gc.

Fig. 6. Weather attenuation at 35 GHz.

Fig. 7A. Theoretical values of attenuation by rain (solid curves) and fog or cloud (dashed curves). Curve (a) 0.25 mm/hr (drizzle), (b) 1 mm/hr (light rain), (c) 4 mm hr (moderate rain), (d) 16 mm hr (heavy rain), (e) 0.032 g/m³ (visibility, 2000 ft), (f) 0.32 g/m³ (visibility, 400 ft), (g) 2.3 g/m³ (visibility, 100 ft).

Fig. 7B. Attenuation due to atmospheric oxygen and water vapor ($x =$ Van Vleck's experimental values); $O_2 + 1\% H_2O$.

Fig. 8. Attenuation (absorption; relatively little scattering of beam) versus frequency. (A) logarithmic plot, (B) linear plot. At sea level, standard temperature and pressure, 1% humidity.

Fig. 9. Influence of sky temperature T_i on apparent temperature of asphalt.

Fig. 10. Target temperature as a function of emissivity and sky temperature.

Fig. 11. Typical gross thermal temperature differences for various objects at different times of the day.

Fig. 12. Calculated (a) intensity reflectivity coefficient (reflectance) and (b) emittance for a water surface.

Fig. 13. Effective emissivities of natural surfaces at 16.7 GHz; horizontal polarization.

Fig. 14. Apparent temperatures of surfaces at 19.4 GHz; horizontal and vertical polarizations.

Fig. 15. Typical radiometric temperature.

Fig. 16. Brightness temperature of snow at 37 GHz.

Fig. 17. Comparison of mean radiometric temperatures at 37 GHz; vertical polarization.

Fig. 18. Microwave temperature of several surfaces at 37 GHz.

Fig. 19. Available temperature differentials vs. altitude.

Fig. 20. Review of passive-microwave state of the art; radiometers.

Fig. 21. Terrain scanning geometry.

Fig. 22. T as function of V_g/h .

Fig. 23. Reference temperature T_1 as function of e_b/e .

Fig. 24. Normalized brightness contrast as function of normalized target temperature.

Fig. 25. $\Delta T'''$ as function of altitude for various targets in a fixed background; normal viewing aspect.

Fig. 26. Road intersection geometry.

Fig. 27. $\Delta T'''$ for concrete roads at K_a -band for various conditions.

Fig. 28. $\Delta T'''$ for a river at K_a -band in (A) clear weather and (B) moderate clouds and rain.

Fig. A1. Radiometric contrast as function of overlap of normally circular ideal pencil beam on a half-plane target.

Fig. A2. Rectangular ideal pencil beam scanning rectangular target; parallel rectangular edges.

OBJECT i
(SKY, CLOUDS, ATMOSPHERE, ETC.)

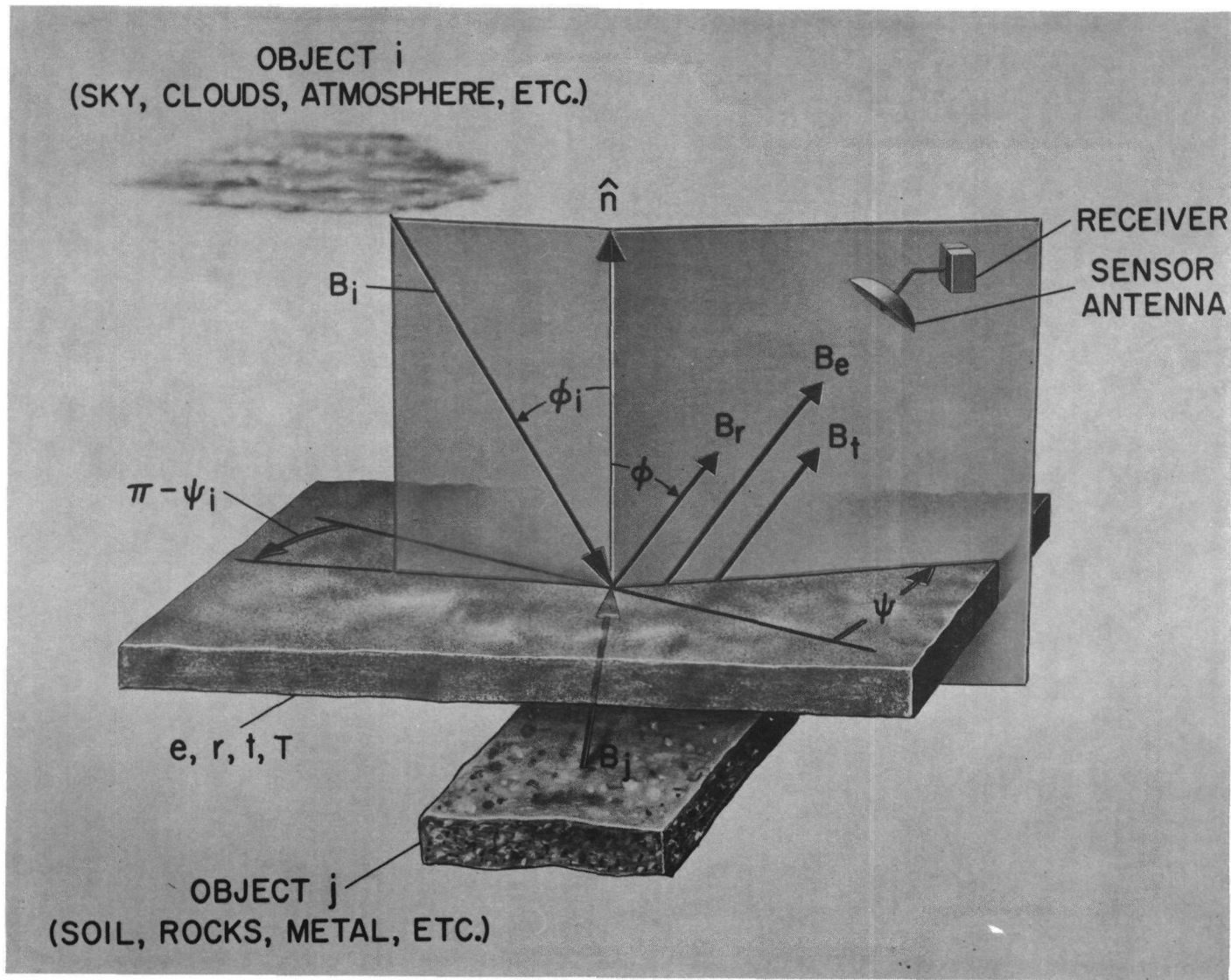


Figure 1.

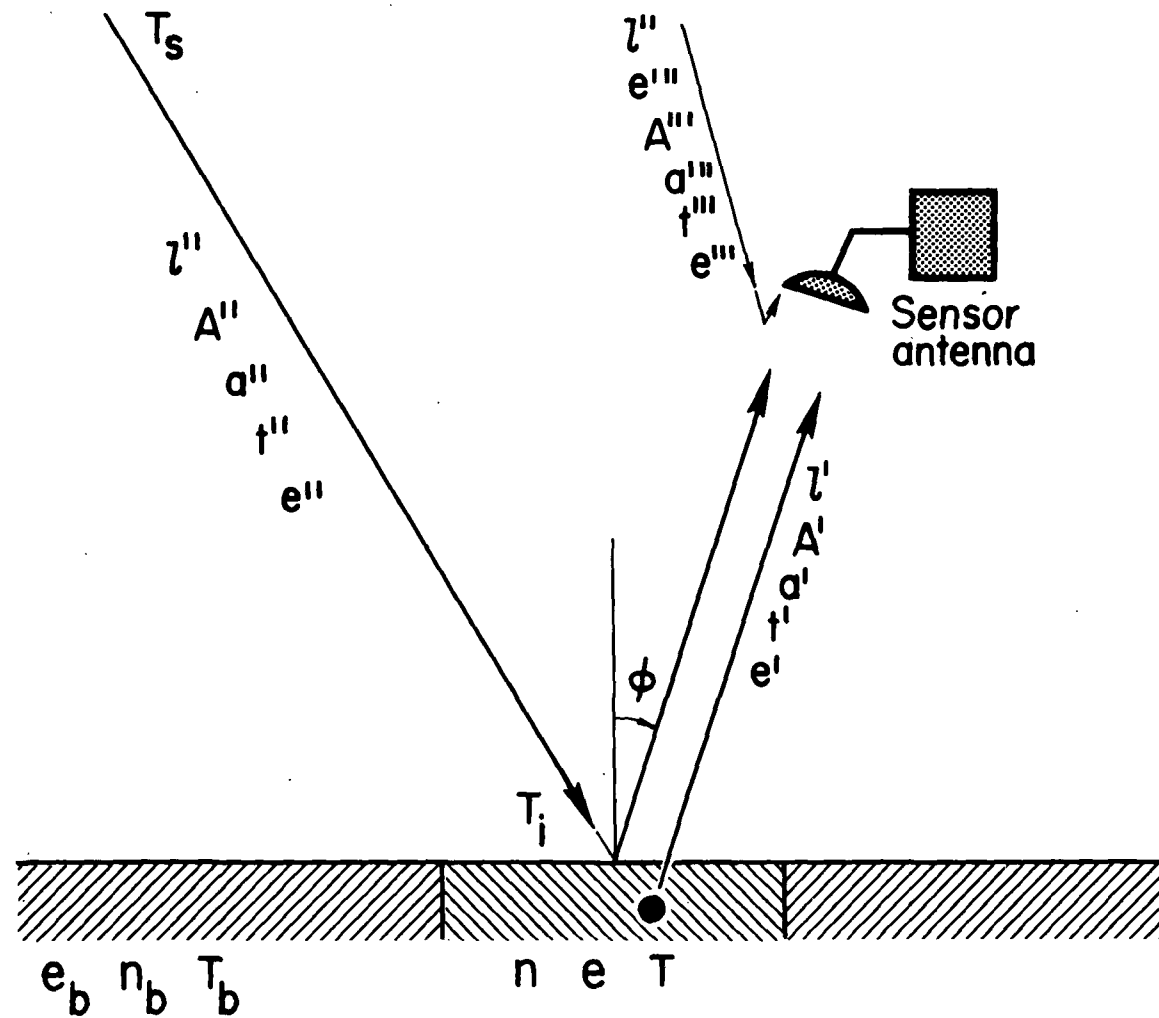


Figure 2

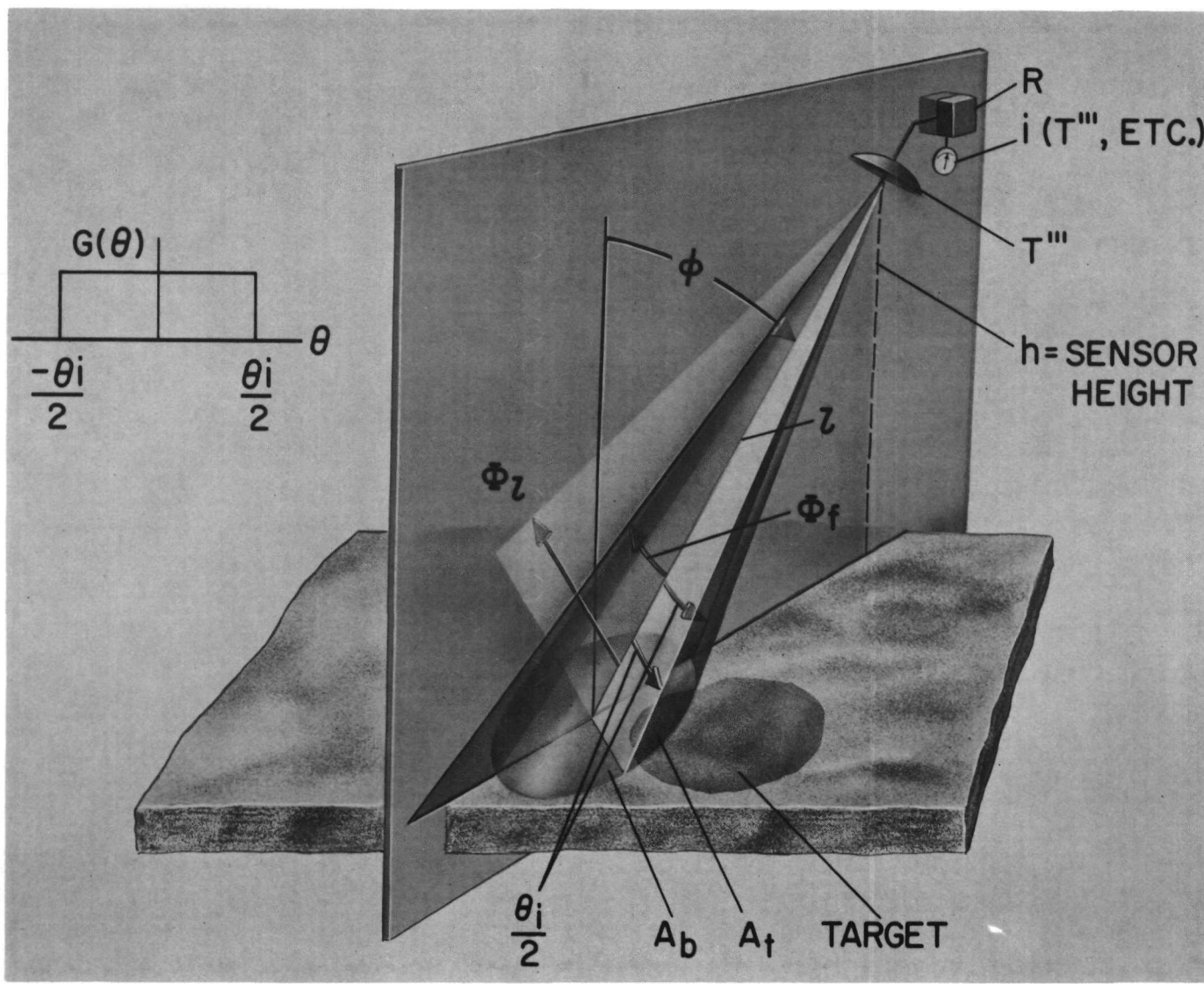


Figure 3.

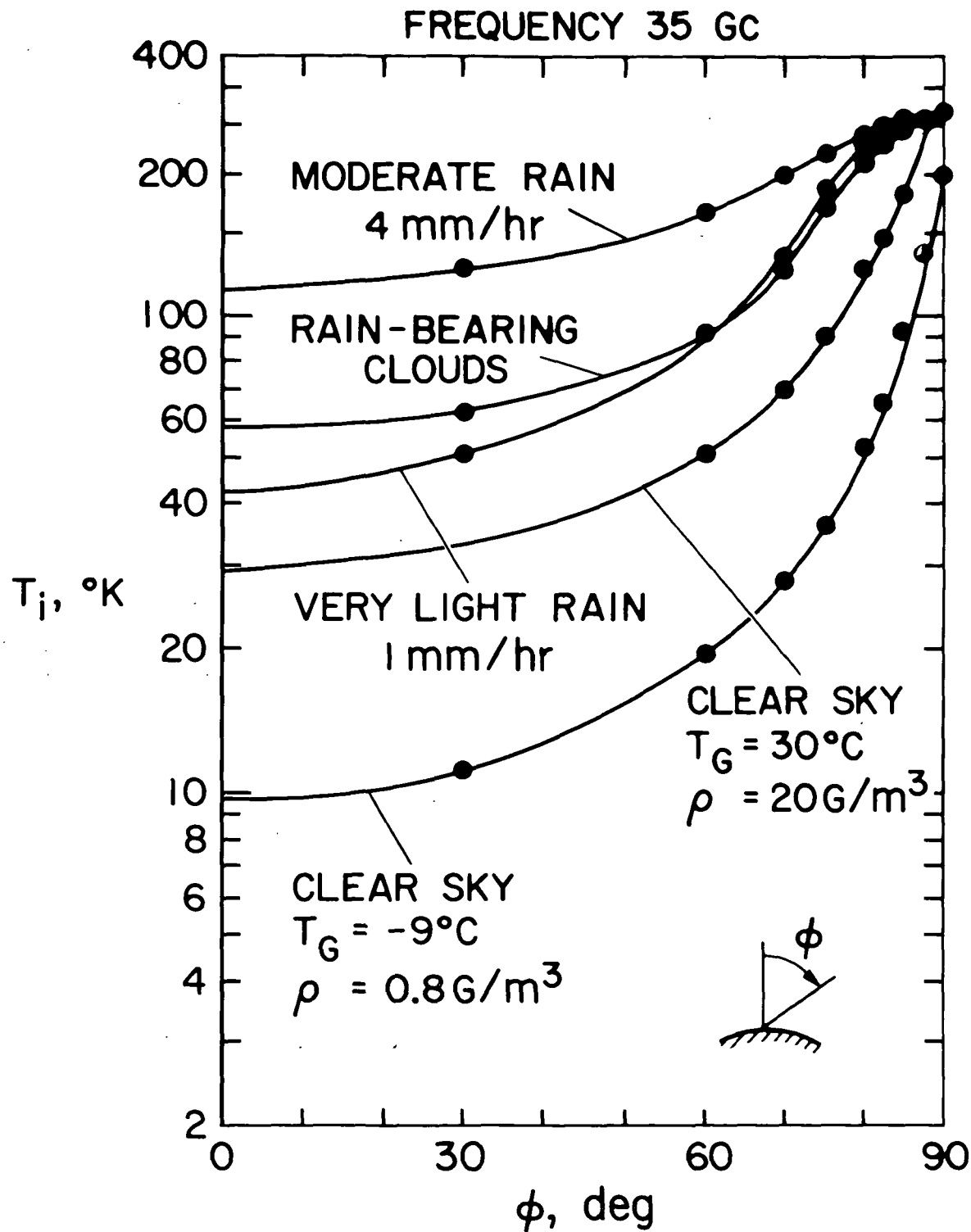


Figure 4

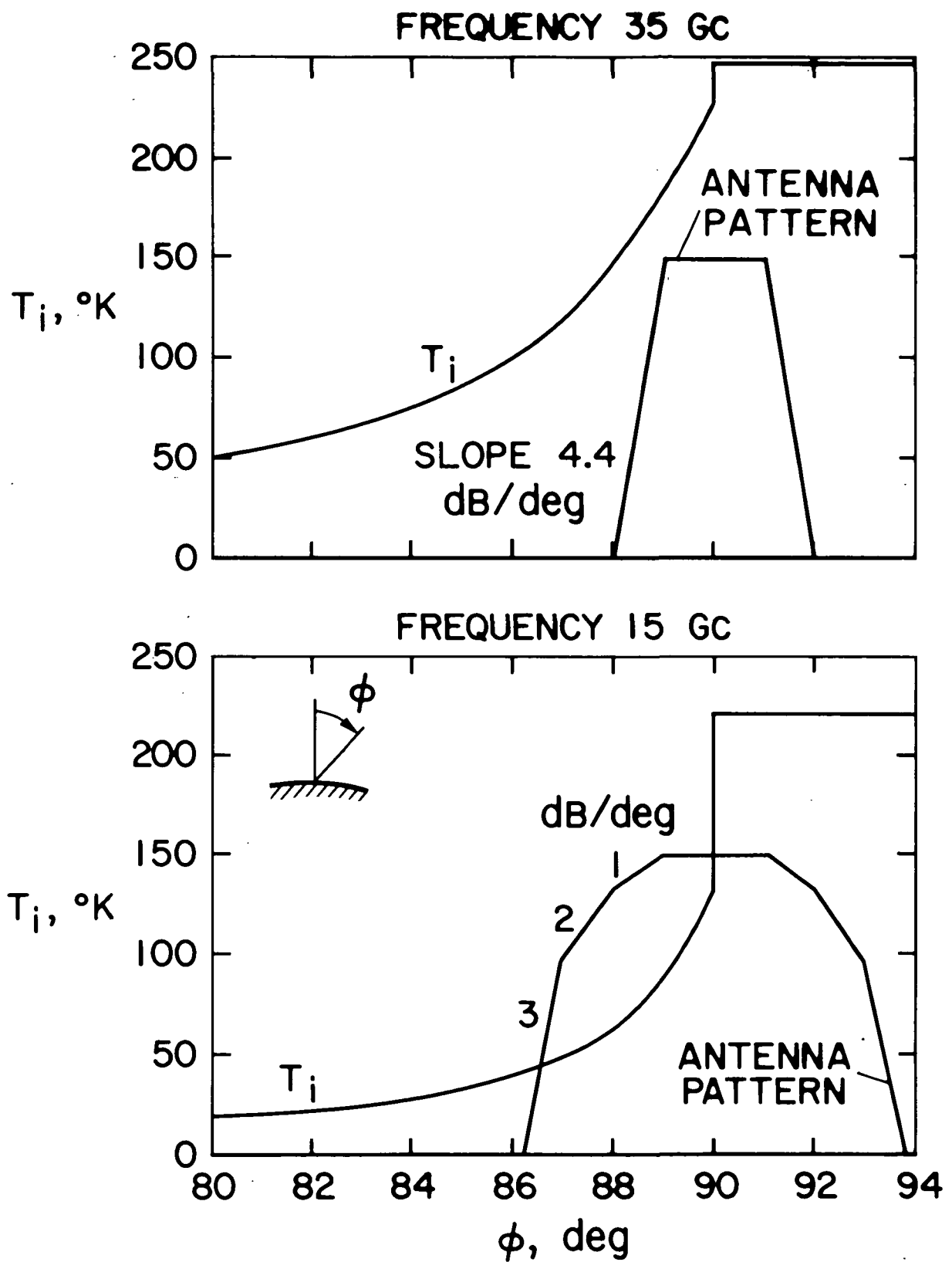


Figure 5

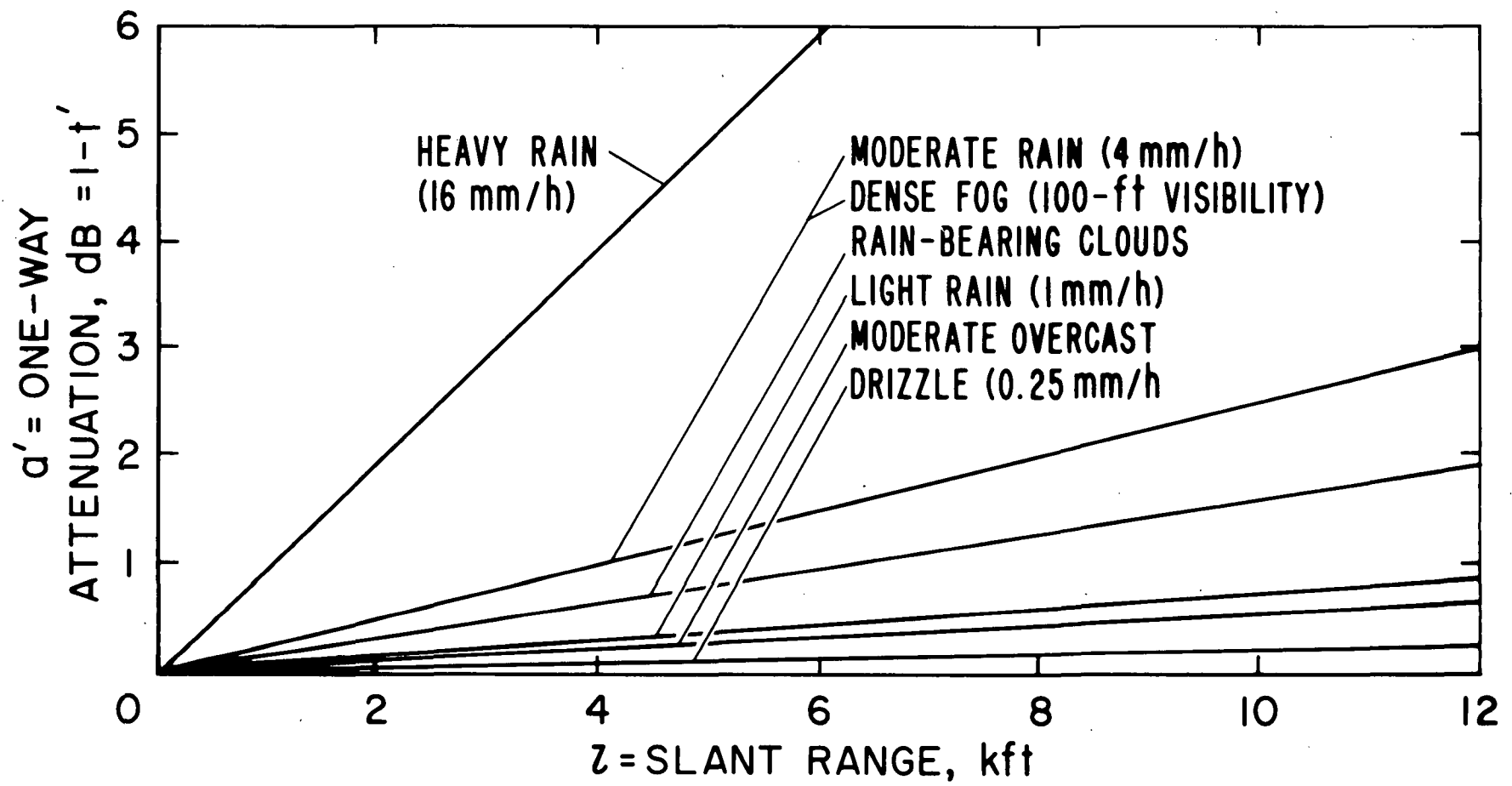
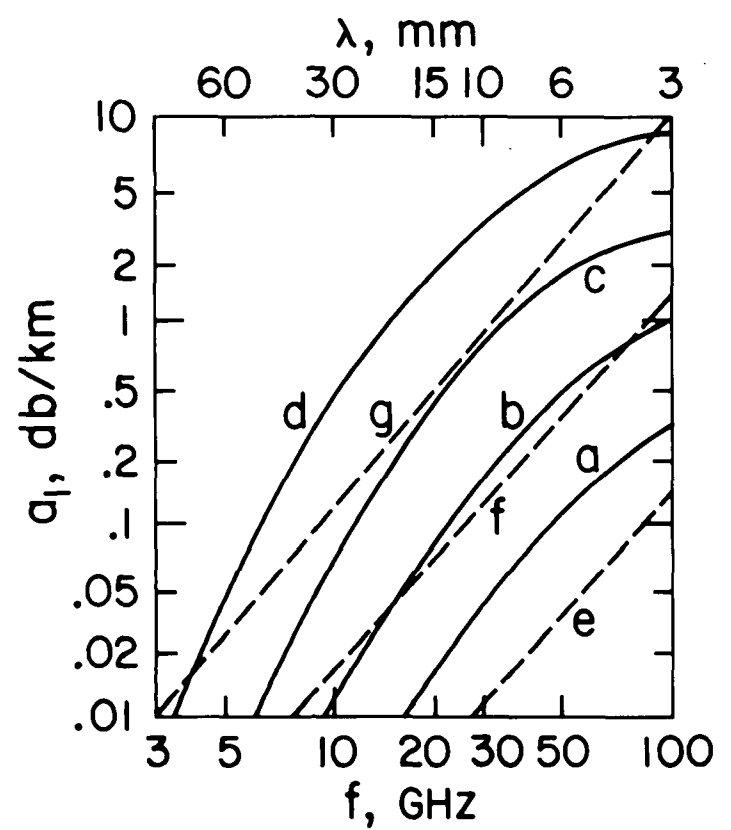
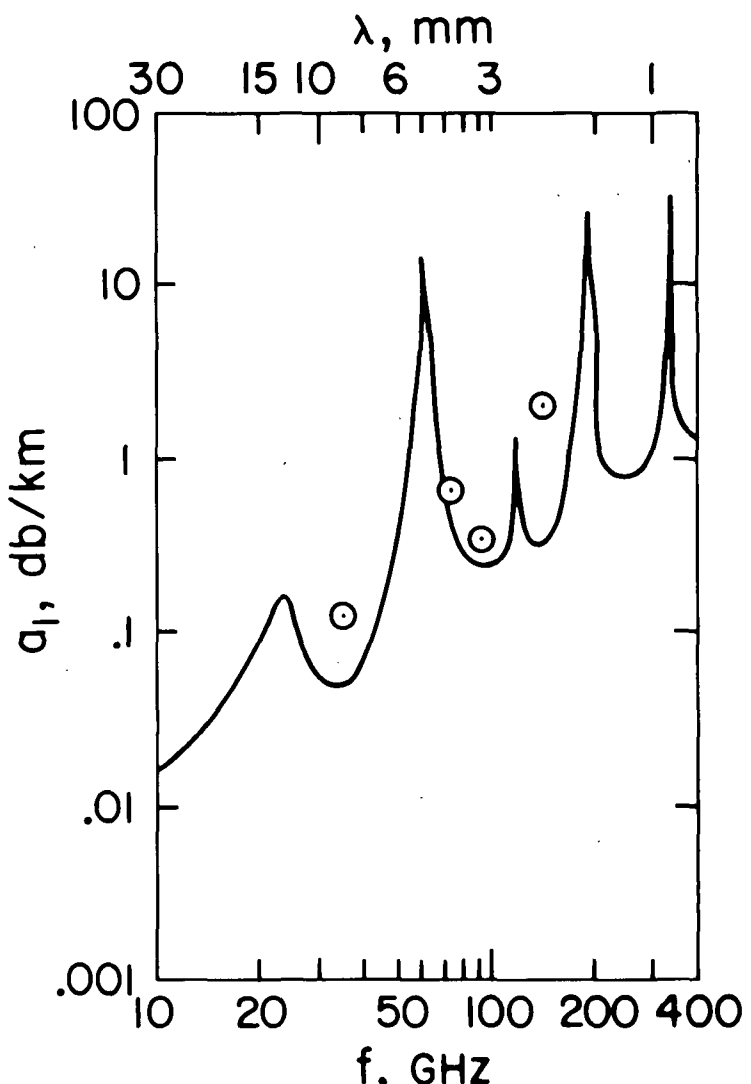


Figure 6



(a)



(b)

Figure 7

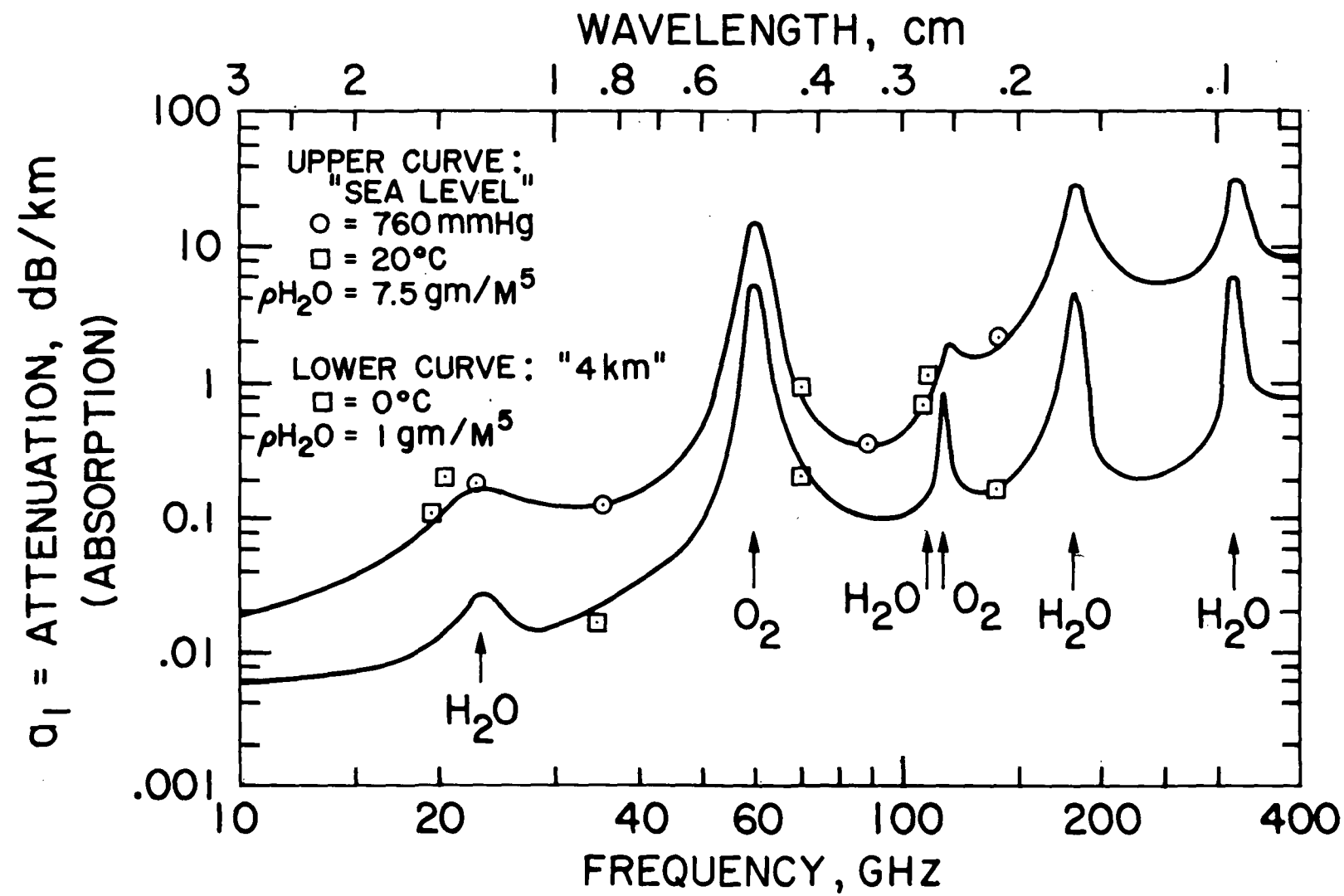


Figure 8a

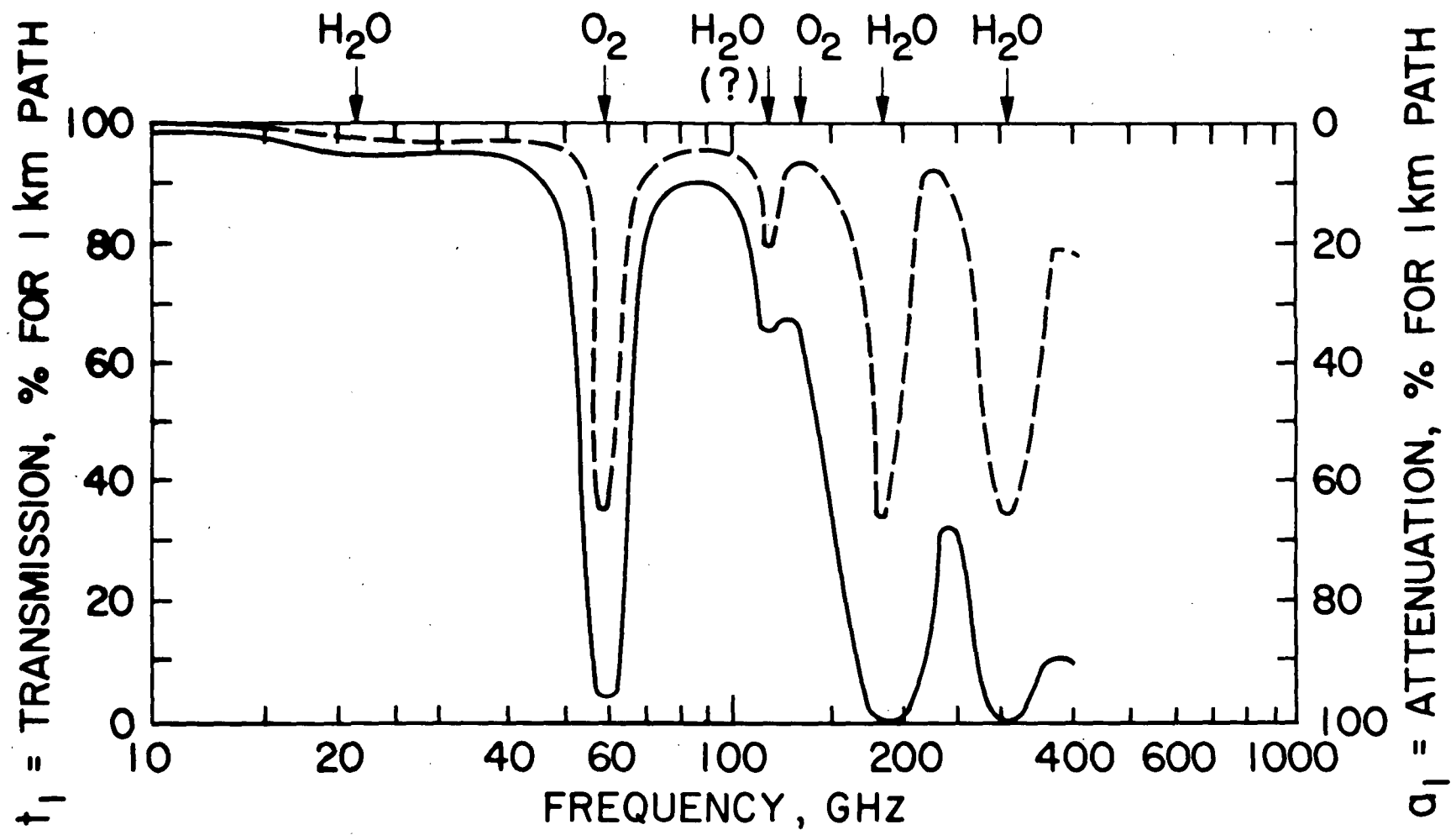


Figure 8b

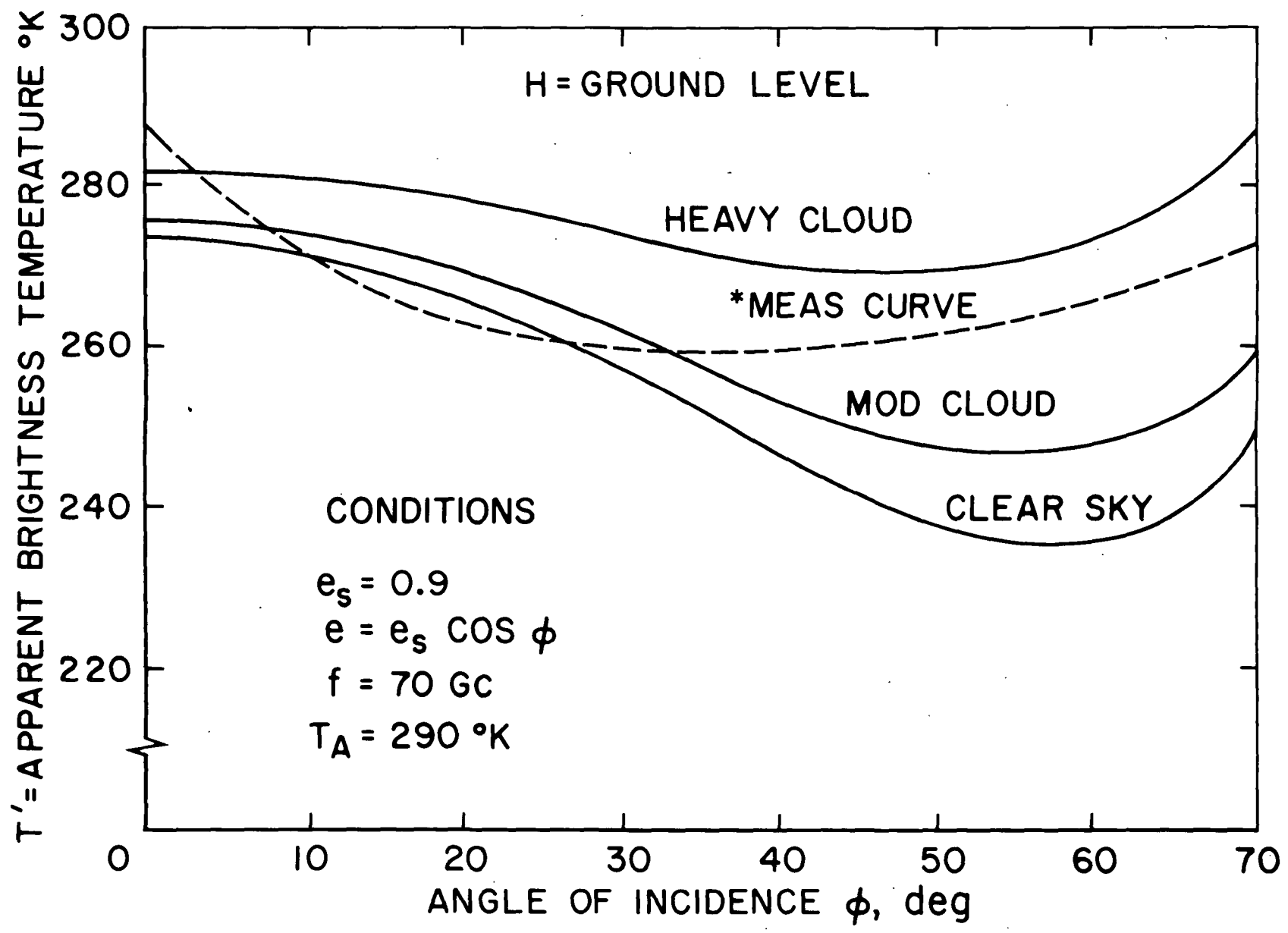


Figure 9

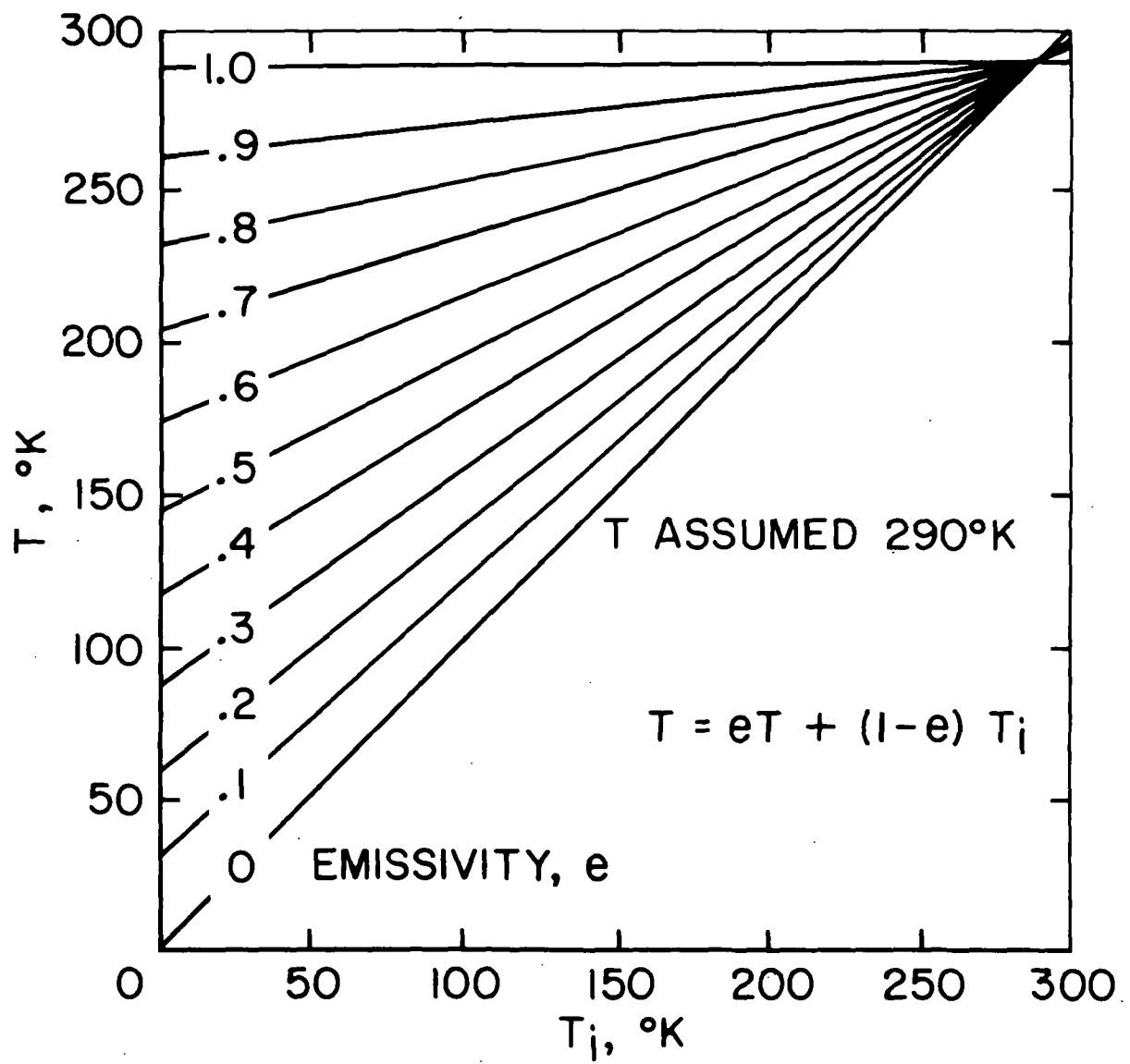


Figure 10

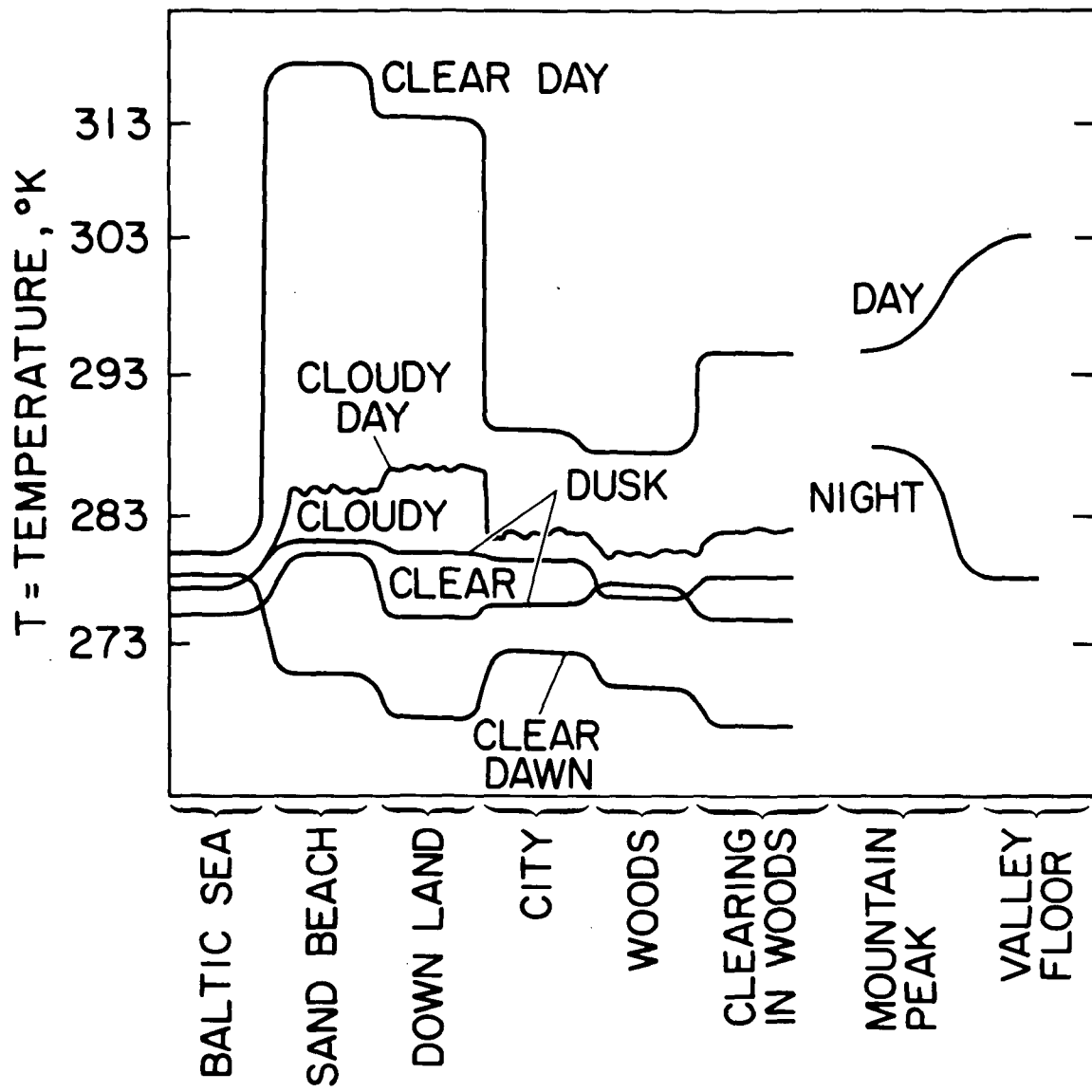


Figure 11

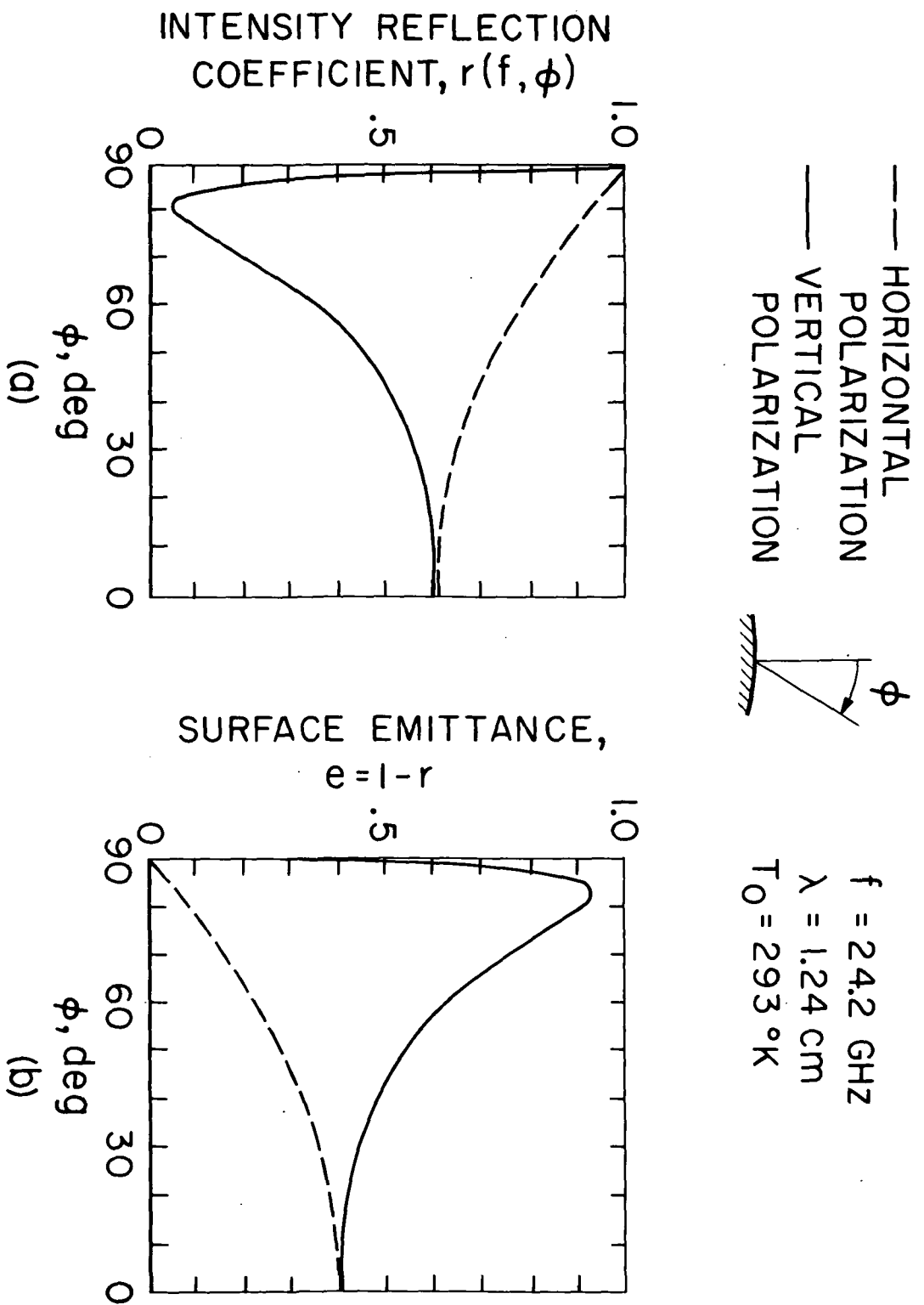


Figure 12

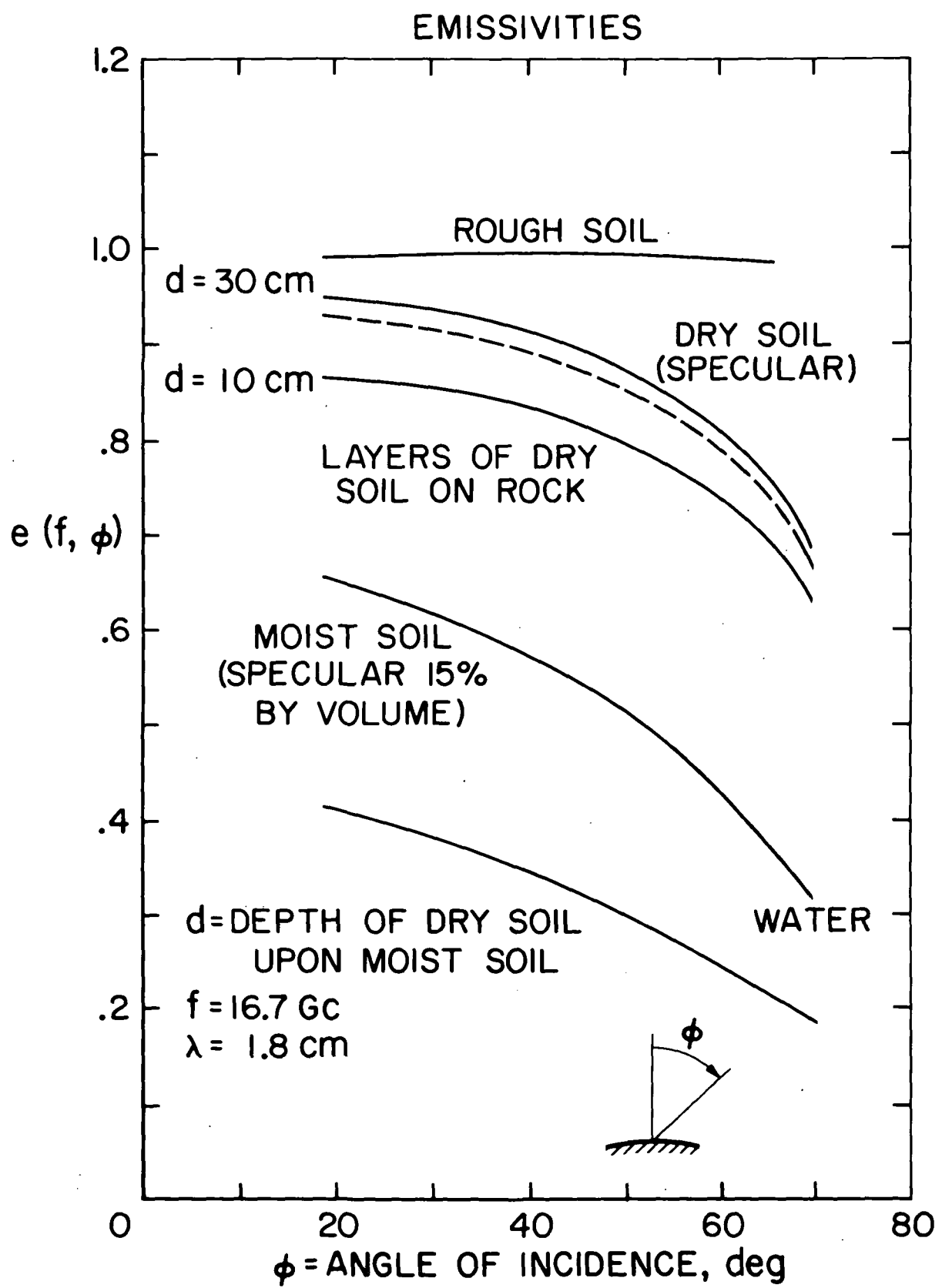


Figure 13

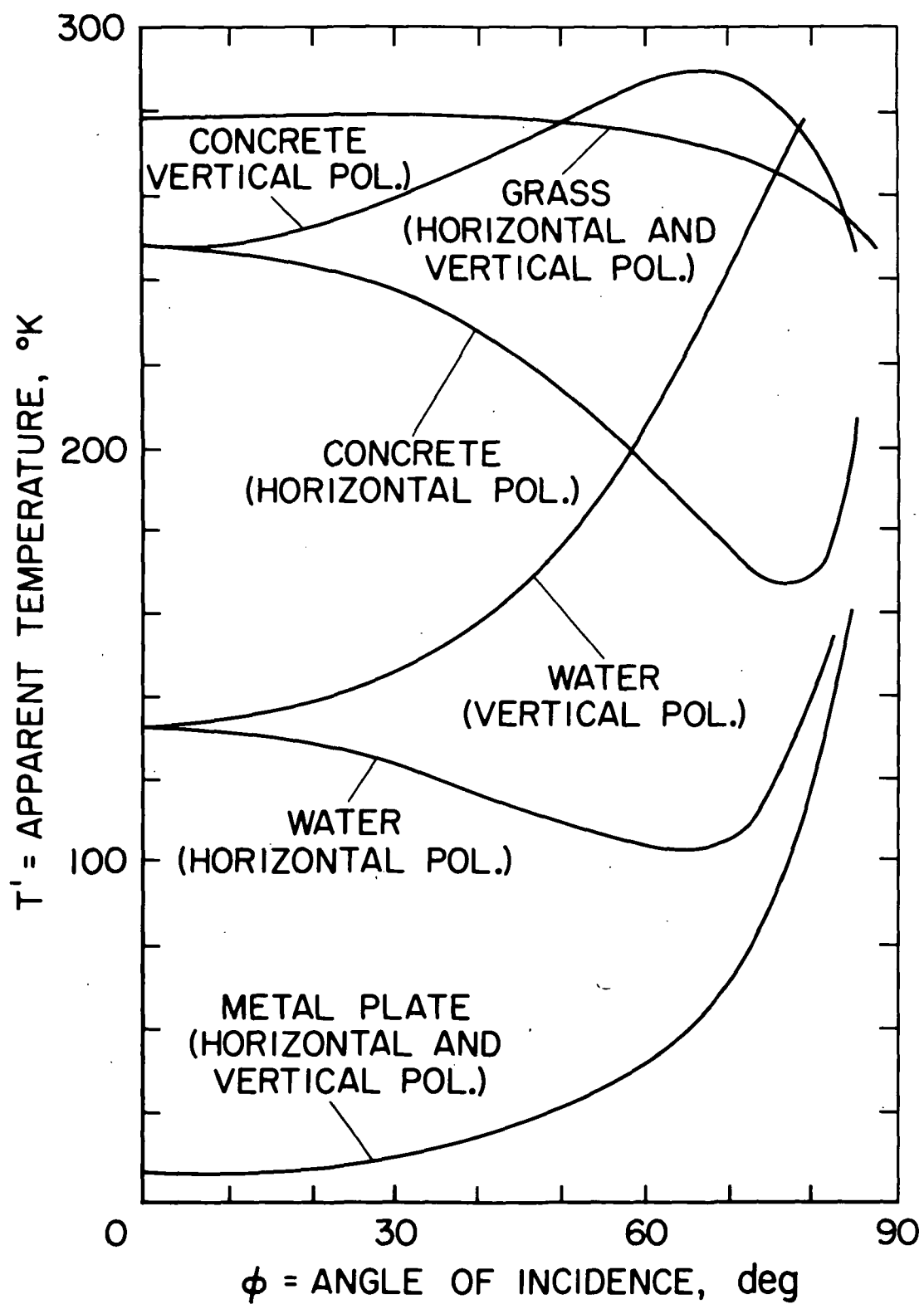


Figure 14

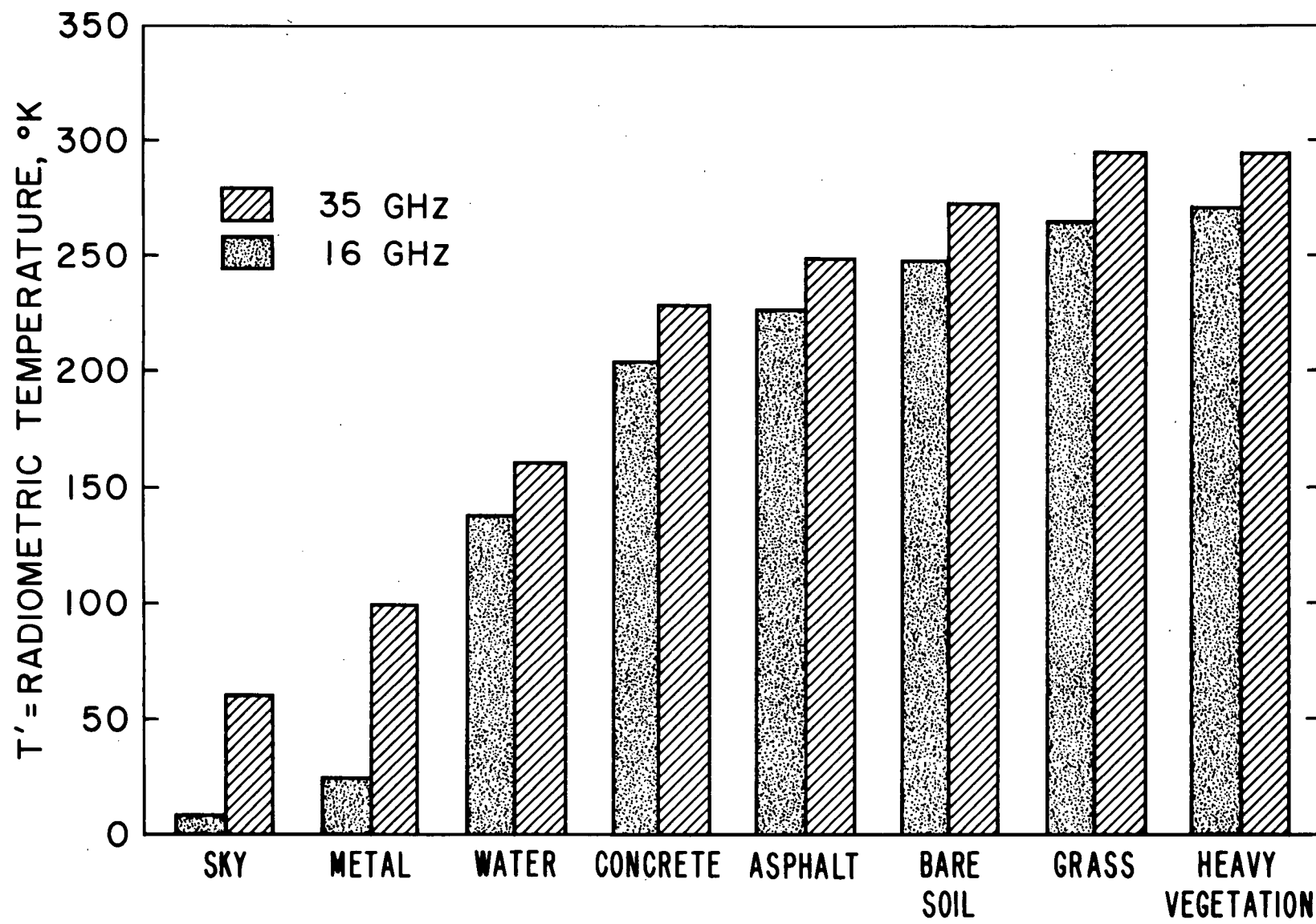


Figure 15

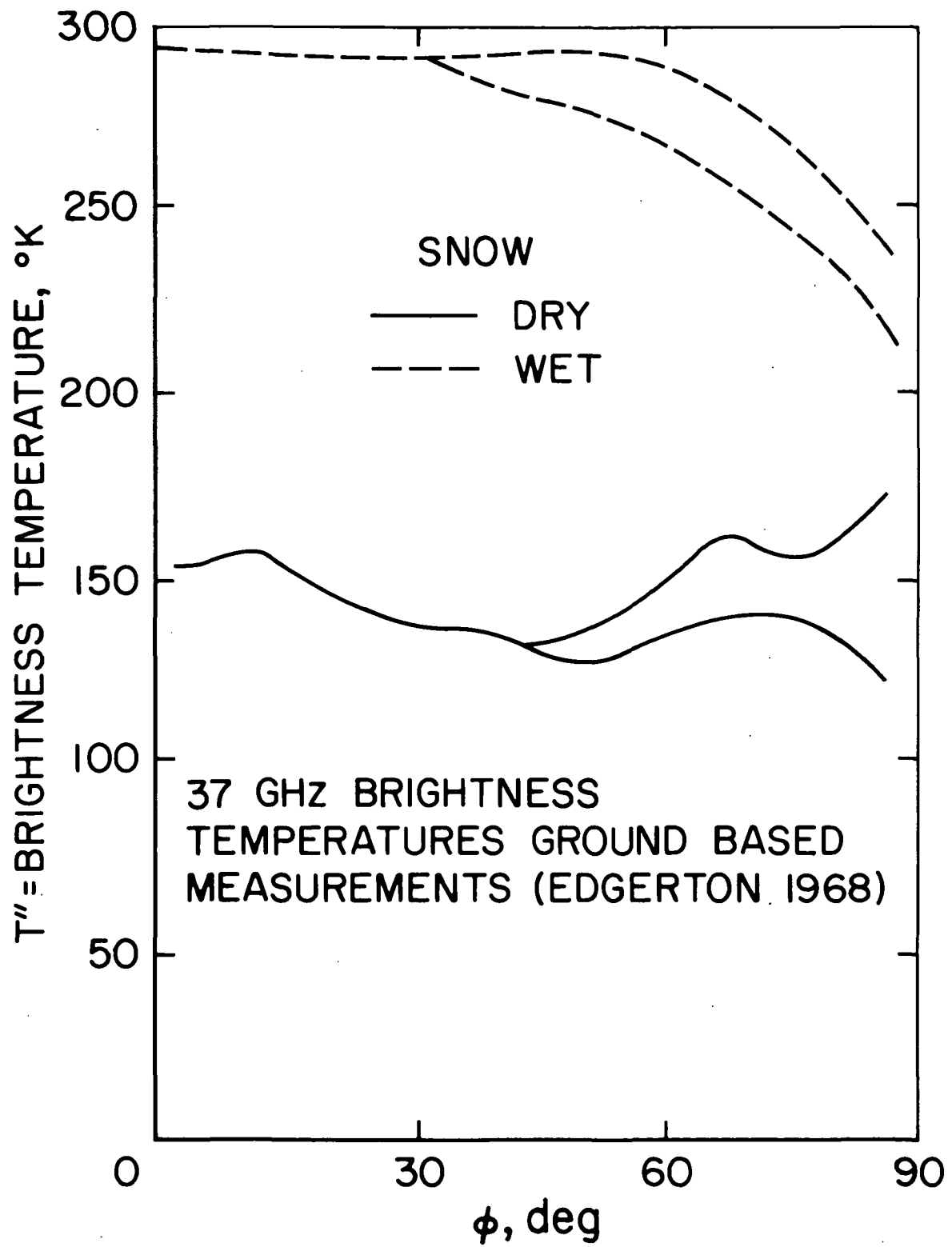


Figure 16

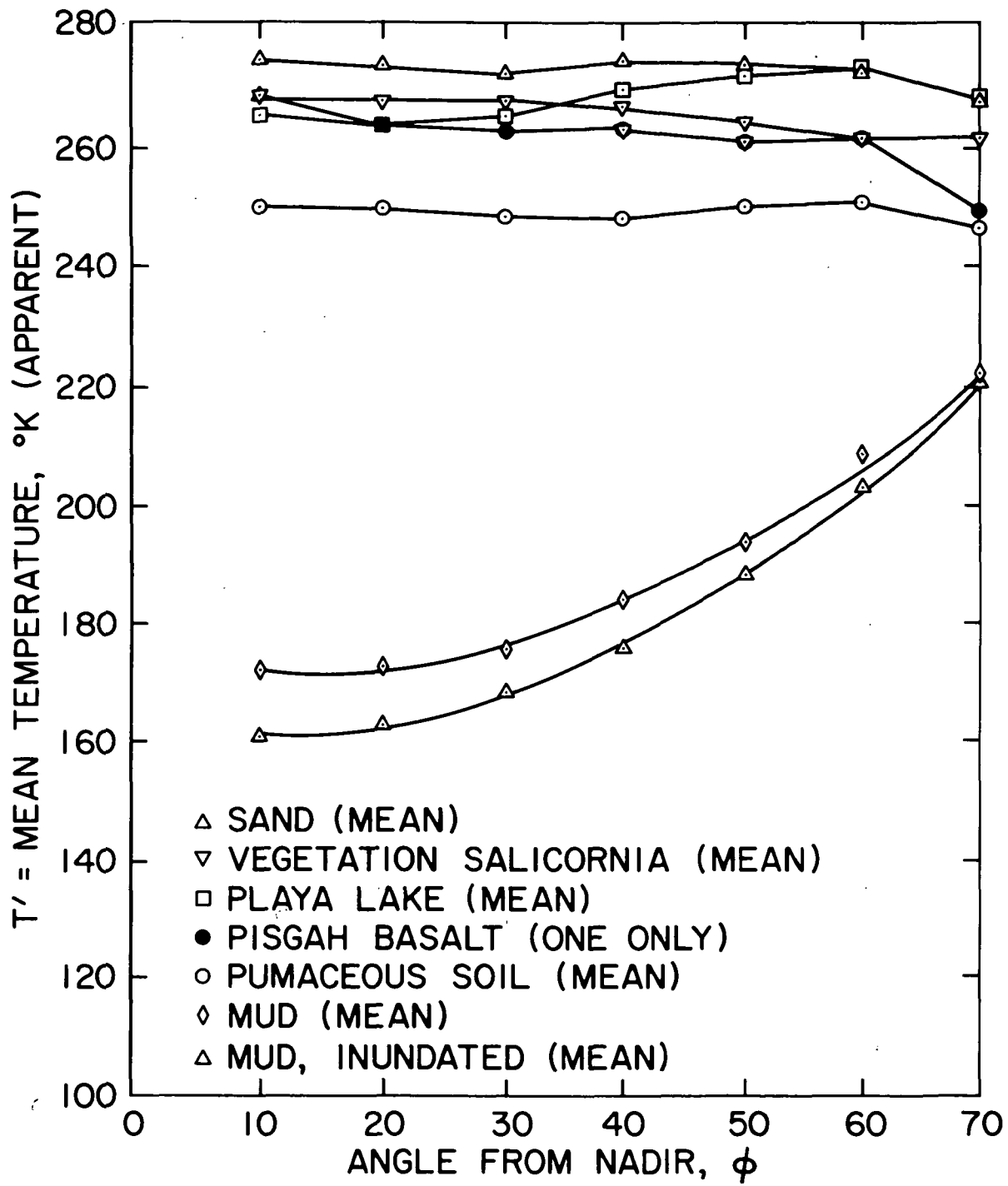


Figure 17

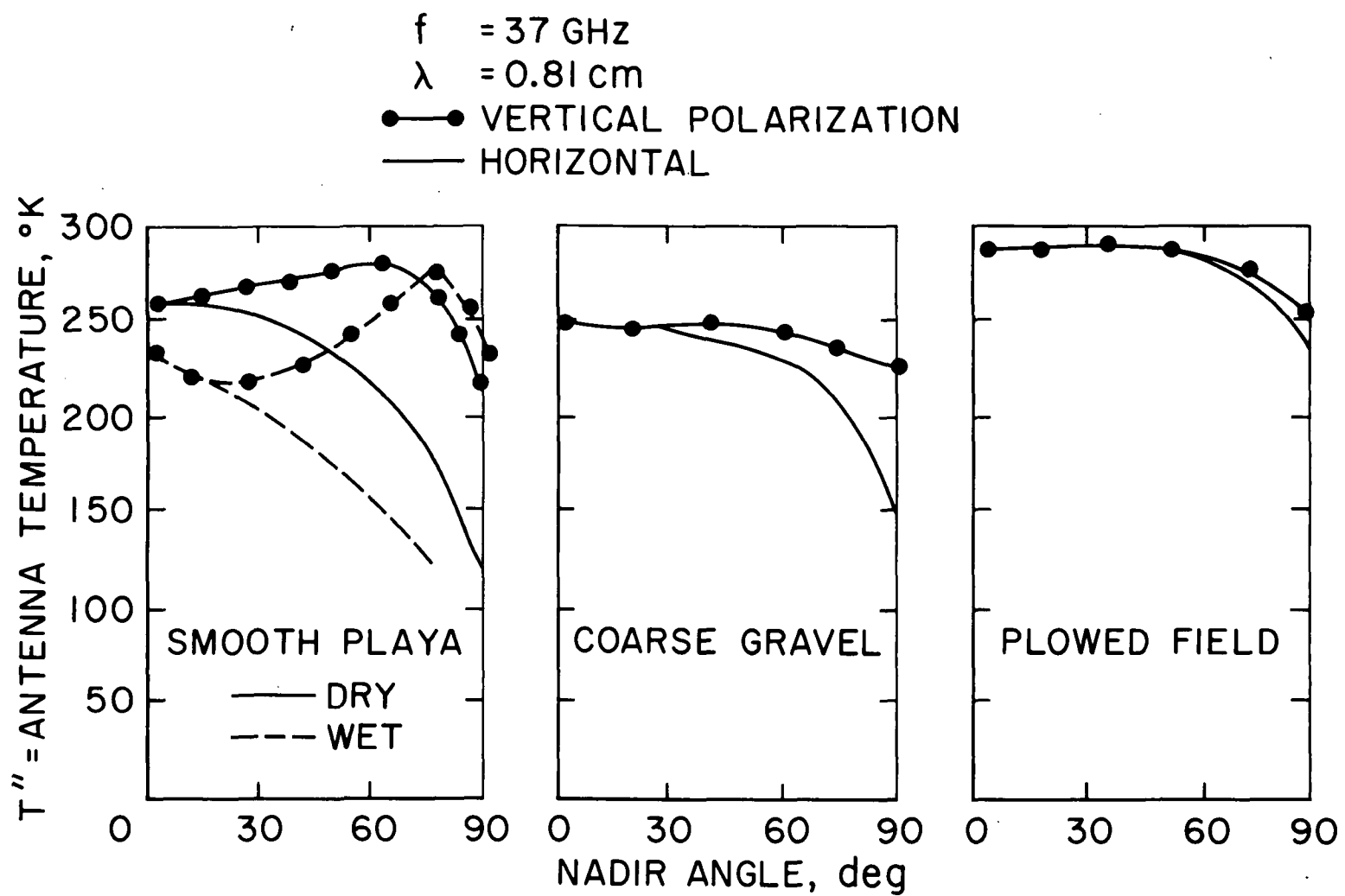


Figure 18

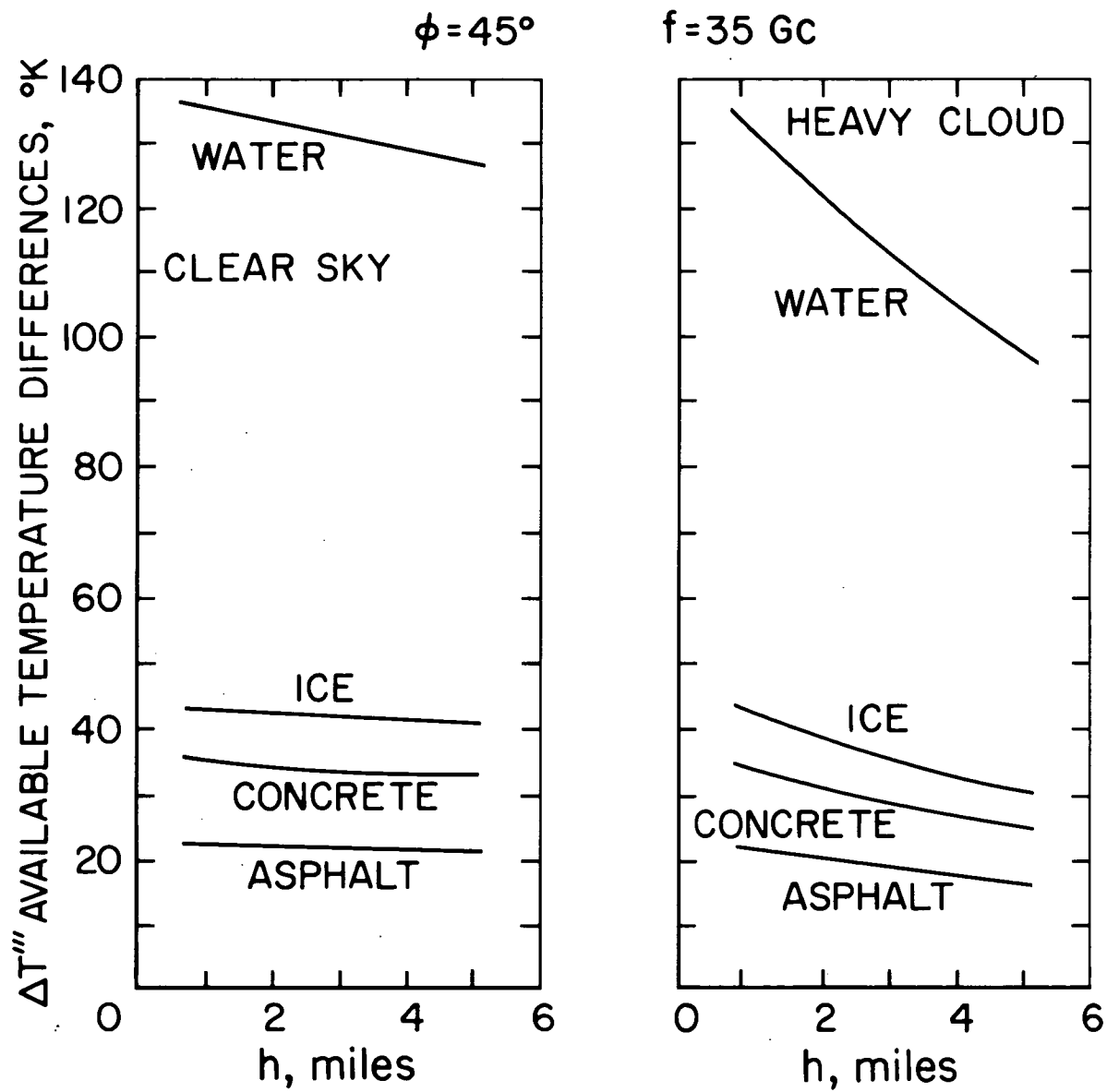


Figure 19

MINIMUM DETECTABLE TEMPERATURE DIFFERENCE,
ST, FOR 1-SECOND INTEGRATION TIME, °K

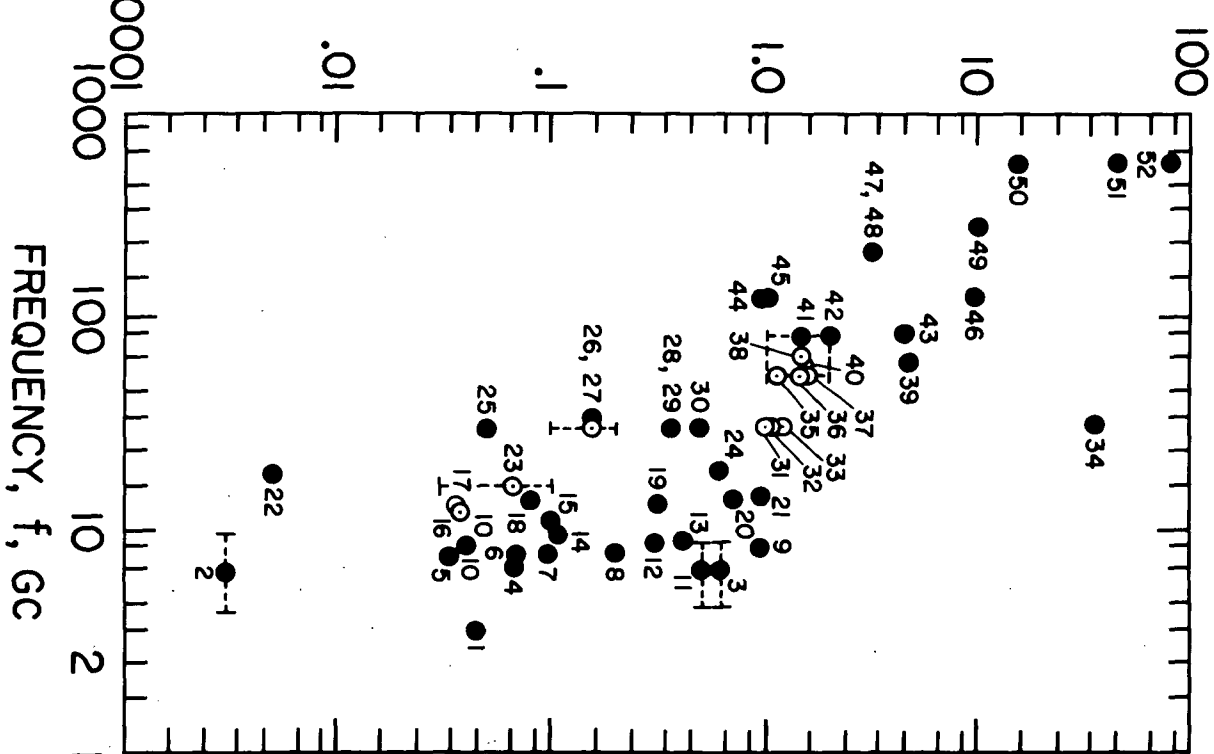


Figure 20

Key to Figure 20

1. Airborne Instrument Laboratories parametric amplifier (in development).
2. Autonetics, Inc. (C. Wiley).
3. North American Aviation (J. Hall).
4. Ewen-Knight Corp. (H. Ewen).
5. University of Michigan parametric amplifier tunnel-diode superheterodyne system (planned).
6. University of Michigan maser (operational).
7. Airborne Instruments Laboratories.
8. Naval Ordnance Laboratory, Corona, Calif.
9. Raytheon (R. Porter).
10. Lear-Siegler, Inc. (D. Mathews).
11. North American Aviation.
12. General Electric.
13. Attainable using tunnel-diode amplifiers.
14. Sperry Microwave Electronics (Mr. Lazarchik).
15. Space General Corp. (T. Falco).
16. Sperry Microwave Electronics (Mr. Lazarchik).
17. Ewen-Knight Corp. (H. Ewen).
18. Collins Radio (W. Bellville).
19. North American Aviation (J. Hall).
20. General Electric.
21. Raytheon (R. Porter).
22. Autonetics, Inc. (T. Falco).

- 23. Space General Corp. (T. Falco).
- 24. Nortronics.
- 25. Airborne Instruments Laboratory.
- 26. Space General Corp. (T. Falco).
- 27. Airborne Instruments Laboratory.
- 28. Ewen-Knight Corp. (H. Ewen).
- 29. Sperry Microwave Electronics (Mr. Lazarchik).
- 30. Martin Co., Orlando, Fla.
- 31. University of Texas.
- 32. General Electric Co.
- 33. Sperry Microwave Electronics (Mr. Lazarchik).
- 34. University of Texas.
- 35. Ewen-Knight Corp. (H. Ewen).
- 36. Collins Radio (W. Bellville).
- 37. Ewen-Knight Corp.
- 38. General Electric Co.
- 39. General Electric Co.
- 40. North American Aviation (J. Hall).
- 41. Space General Corp. (T. Falco).
- 42. Aerospace Corp. (D. King).
- 43. Raytheon (R. Porter).
- 44. U.S. Army Ballistic Research Laboratories, Aberdeen (Md.)
Proving Grounds (K. Richer).
- 45. Electronic Communications, Inc.
- 46. Royal Radar Establishment.

47. Electronic Communications, Inc.
48. U.S. Army Ballistic Research Laboratories, Aberdeen (Md.)
Proving Grounds (K. Richer).
49. Space General Corp.
50. Department of the Army, Frankfort Arsenal.
51. U.S. Army Ballistic Research Laboratories, Aberdeen (Md.)
Proving Grounds (K. Richer).
52. Advanced Technology, Inc.

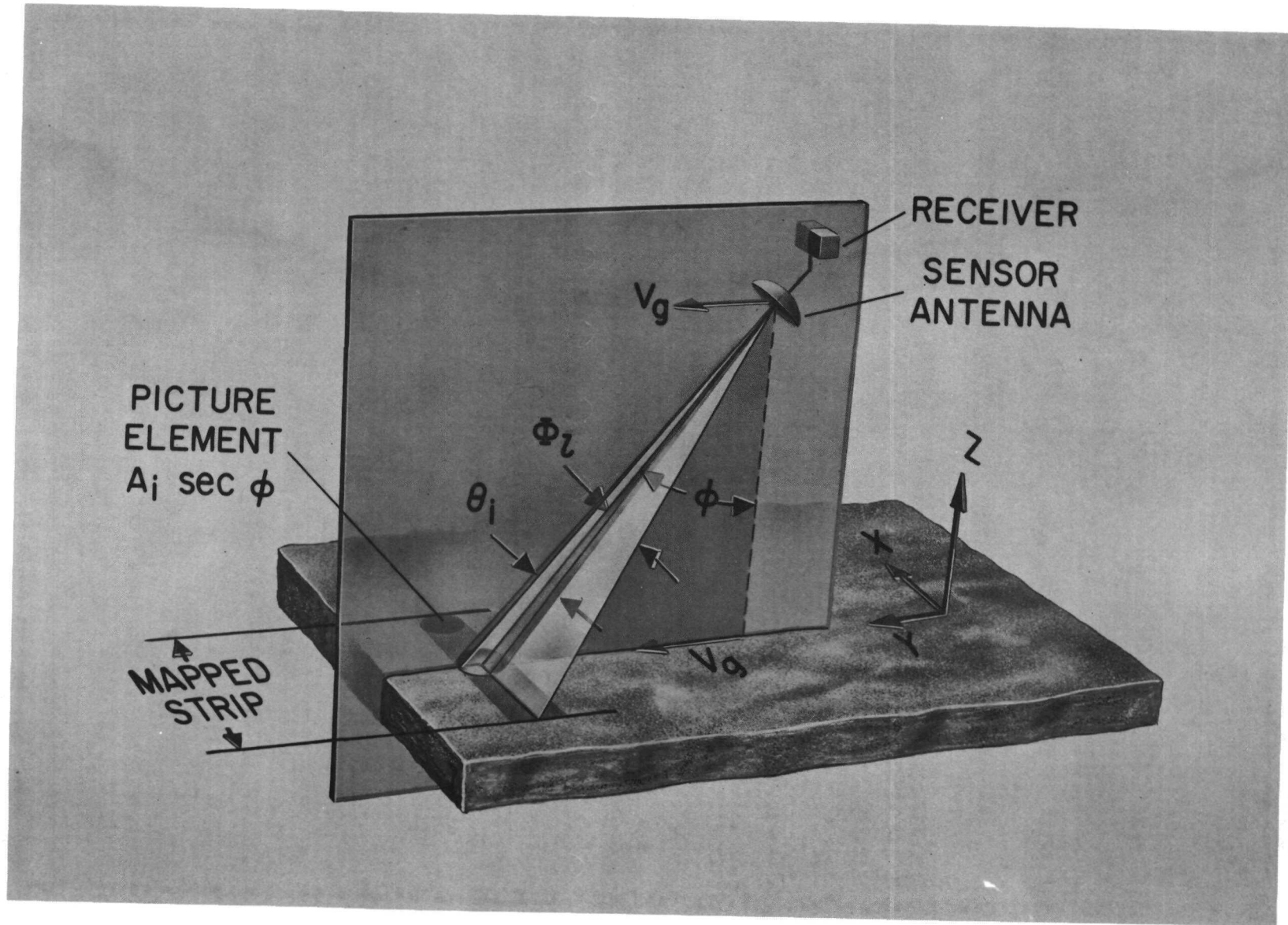


Figure 21.

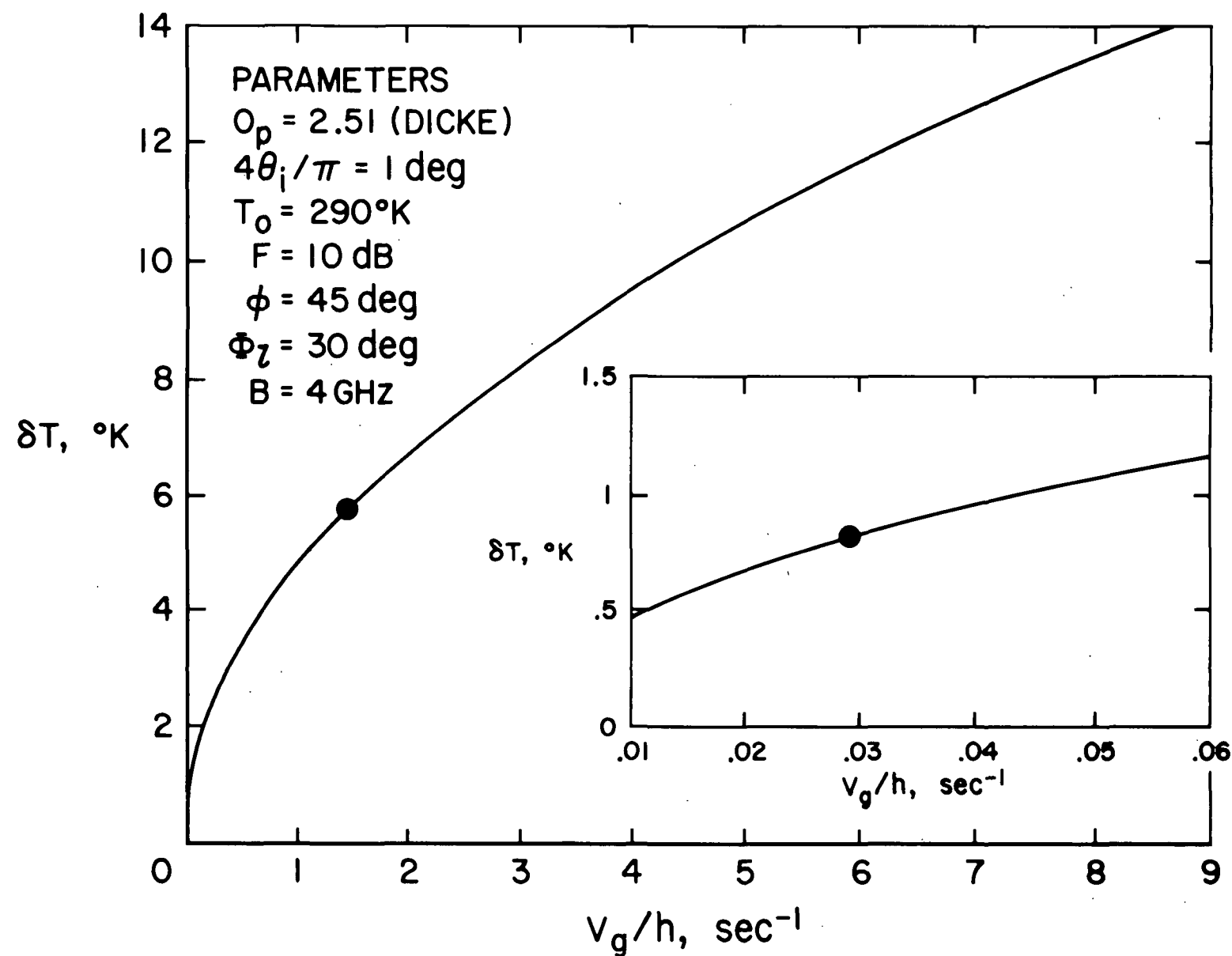


Figure 22

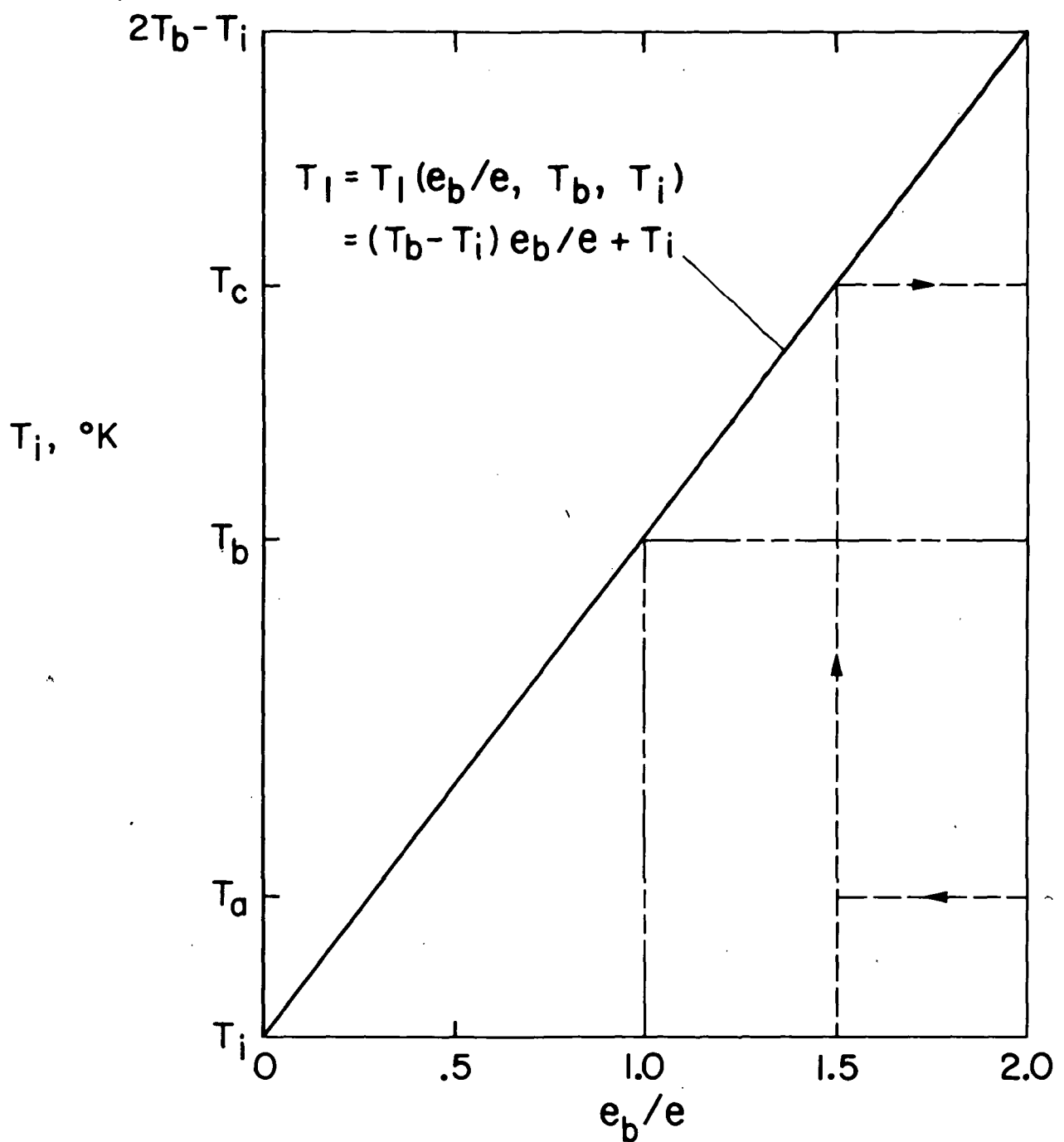


Figure 23

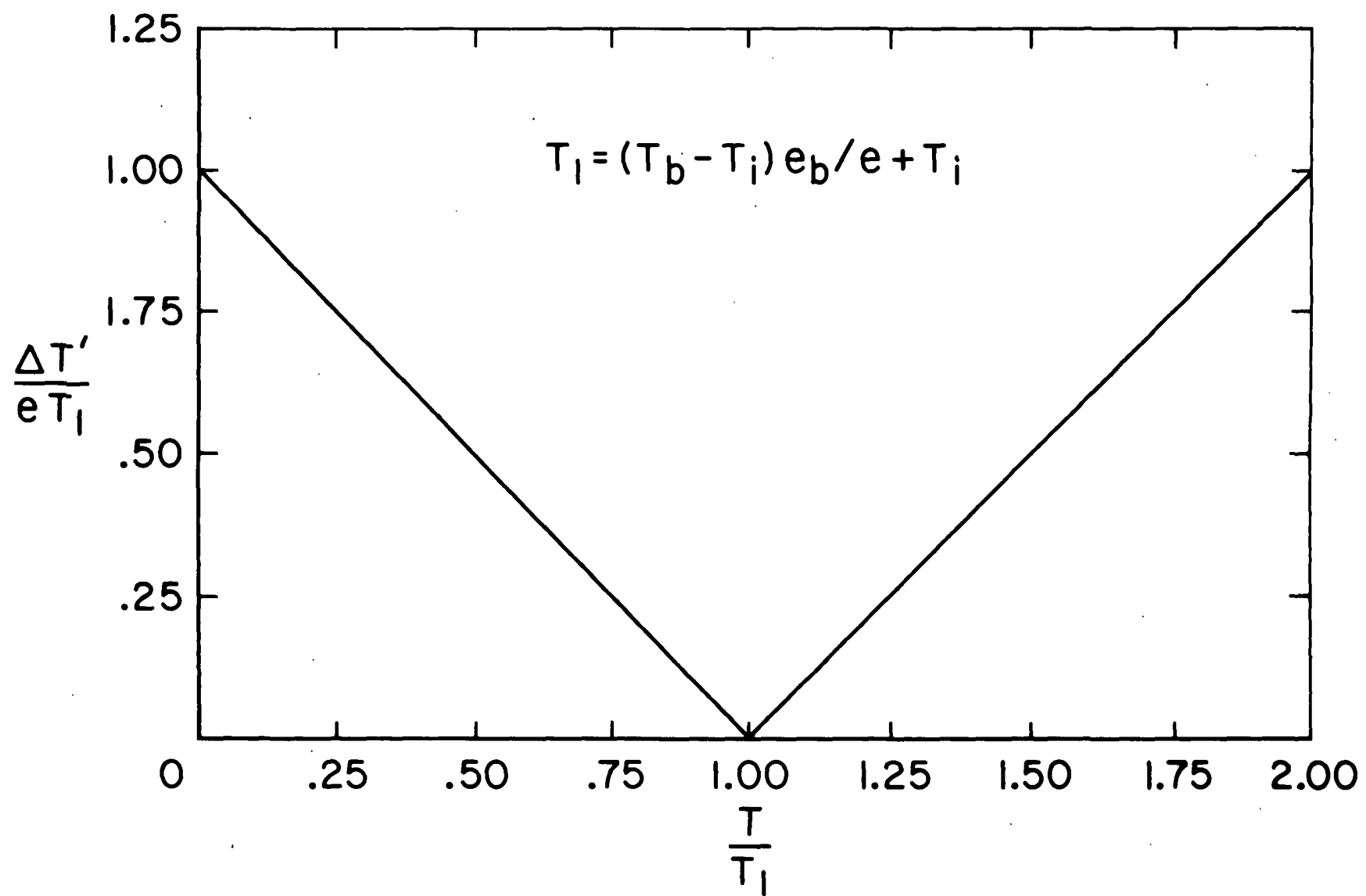


Figure 24

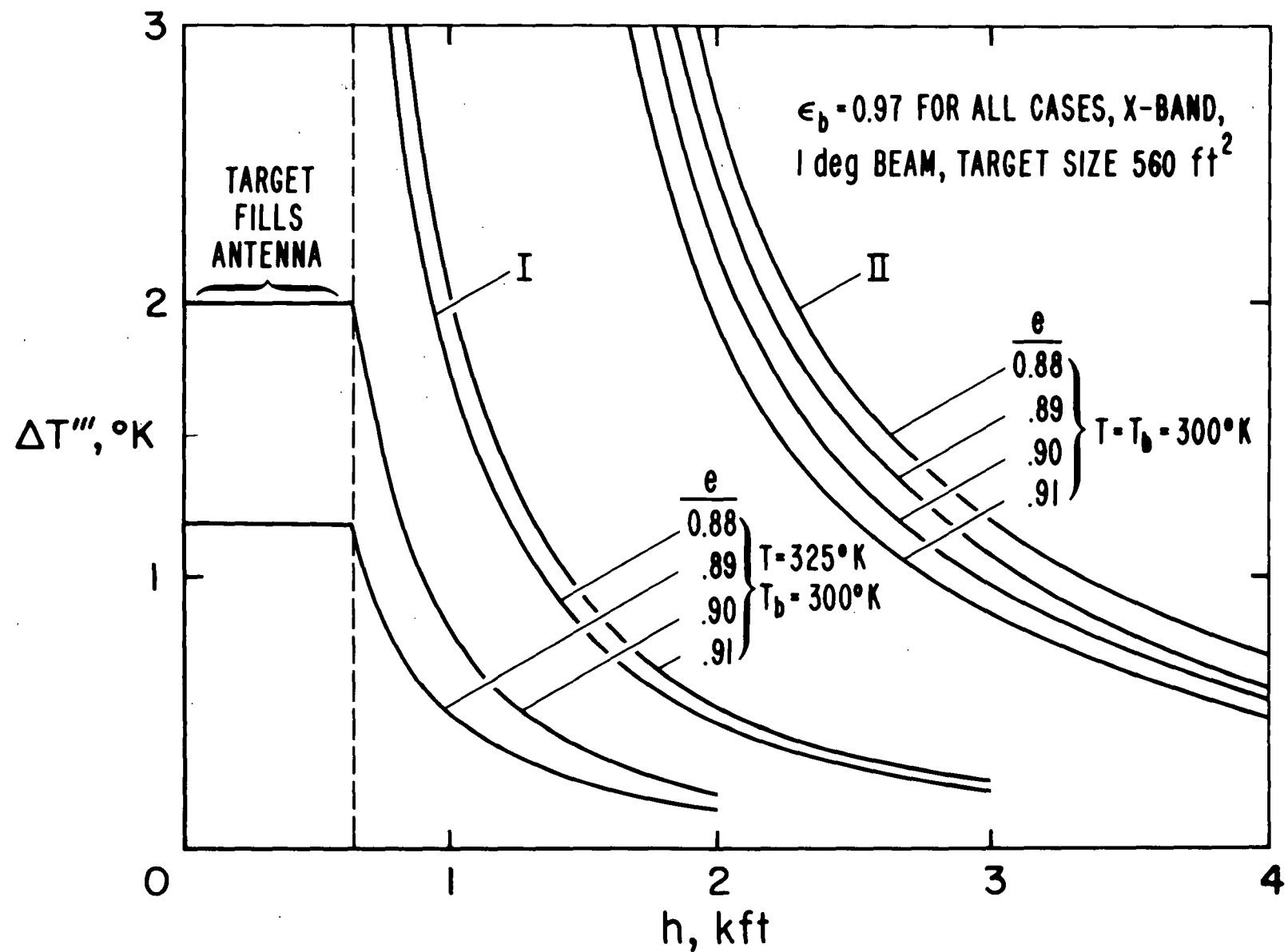


Figure 25

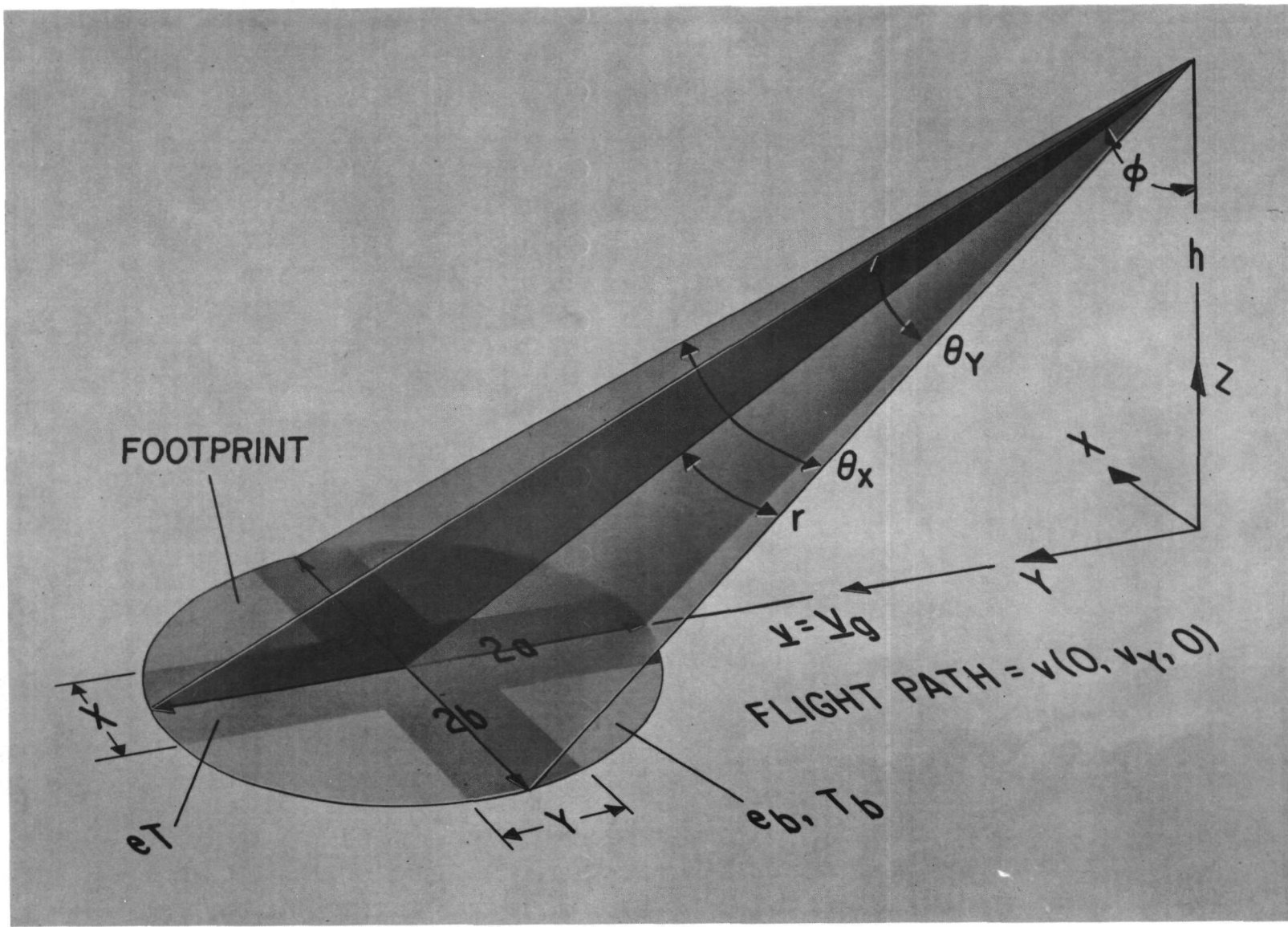


Figure 26.

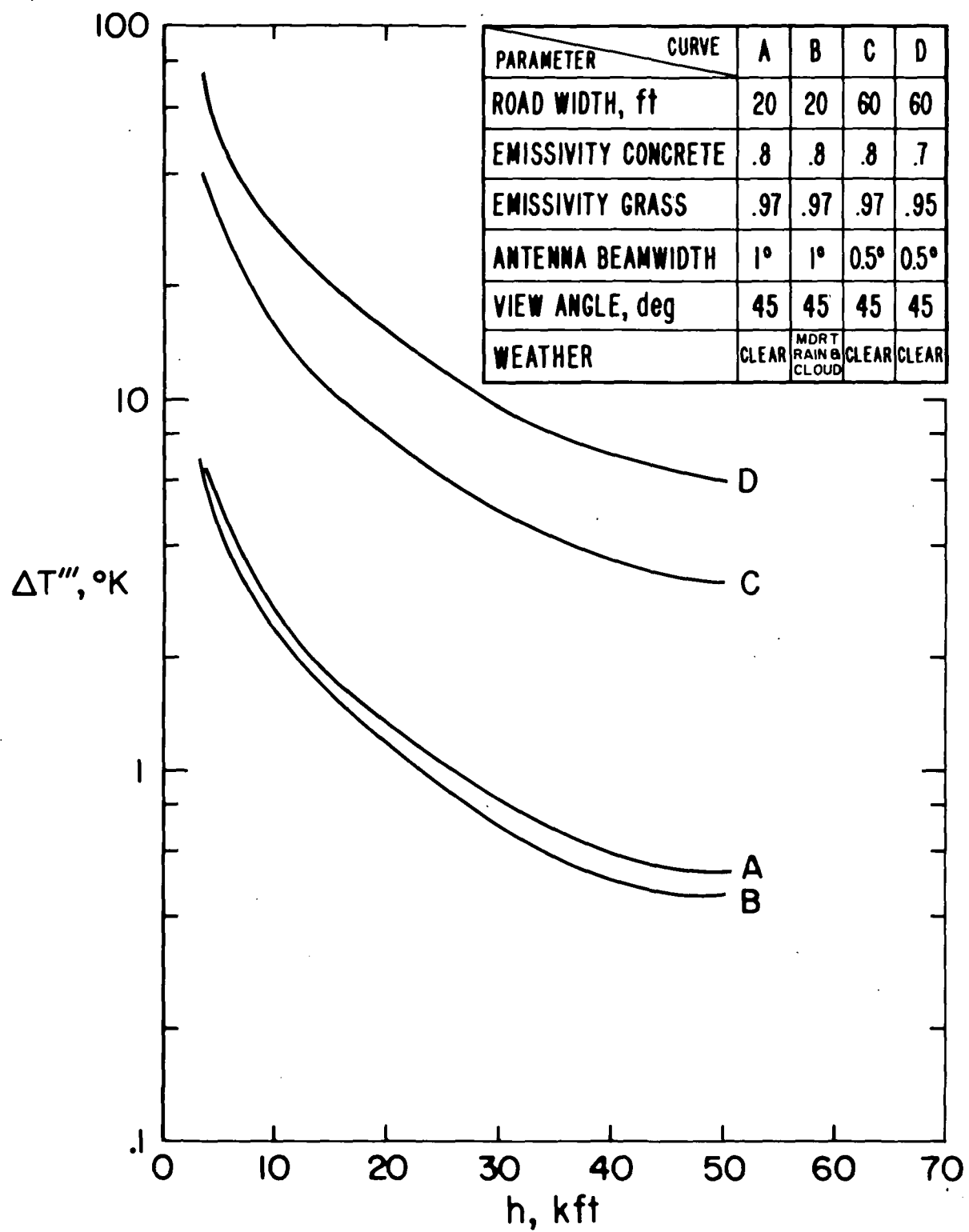


Figure 27

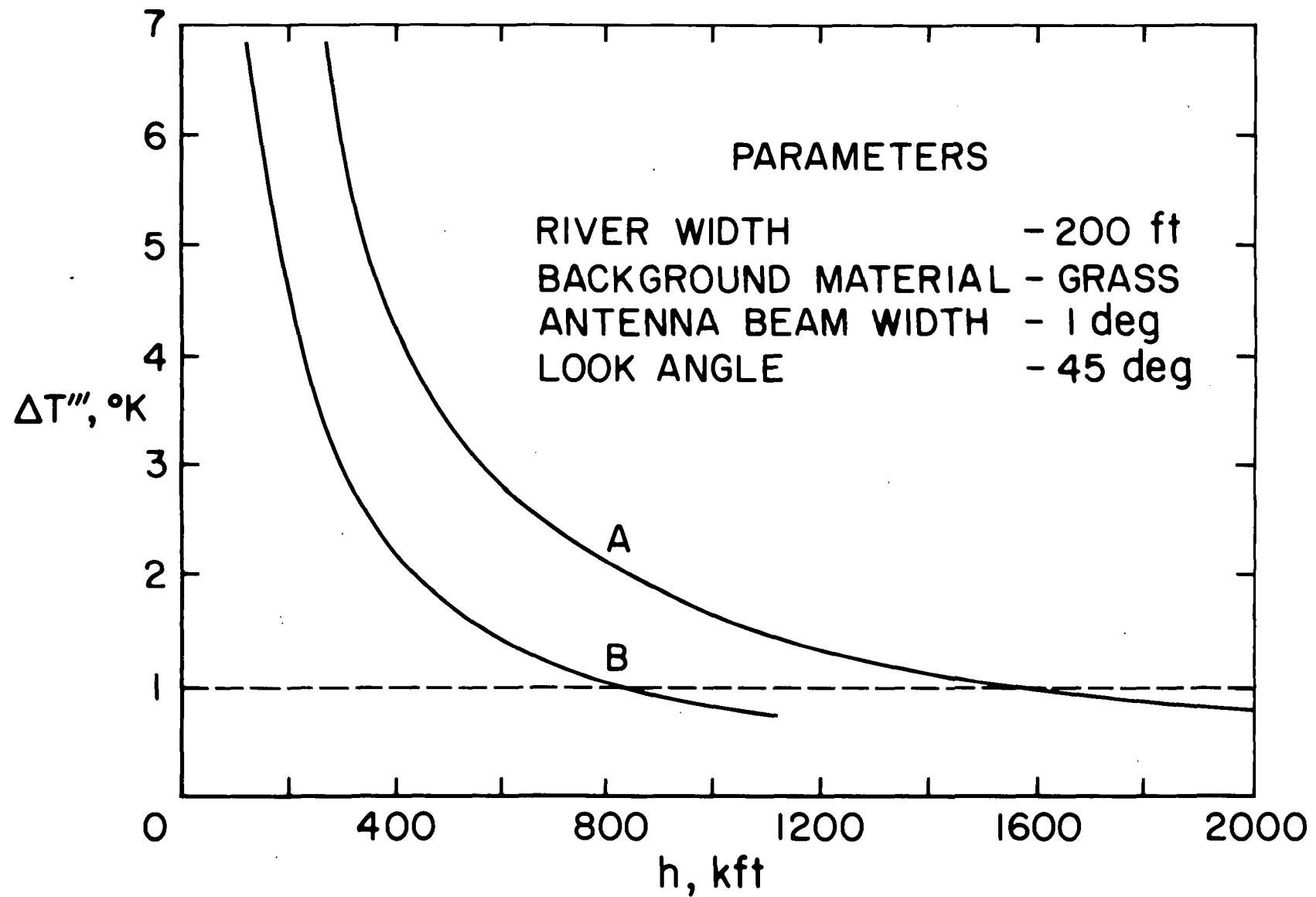


Figure 28

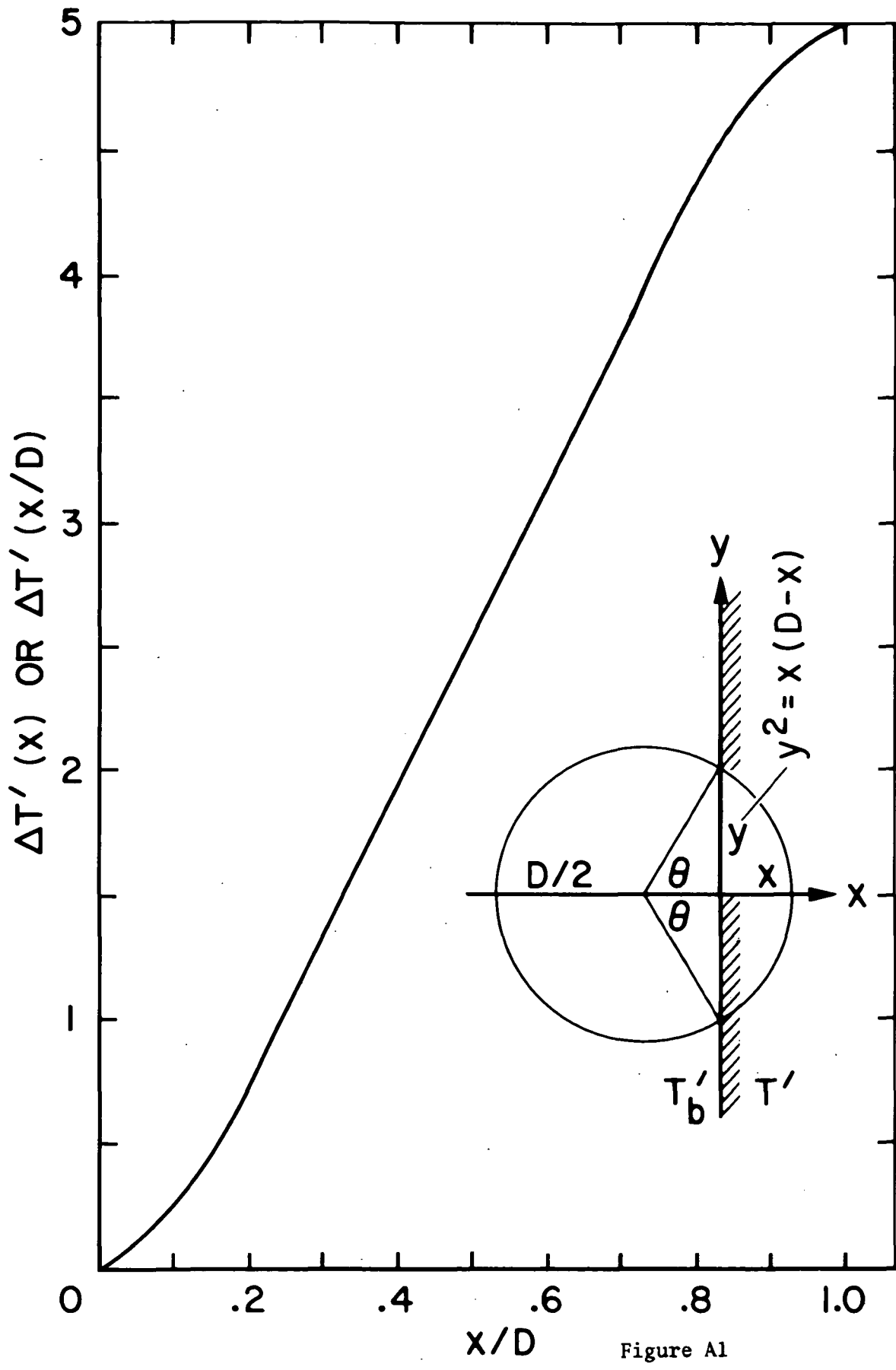


Figure A1

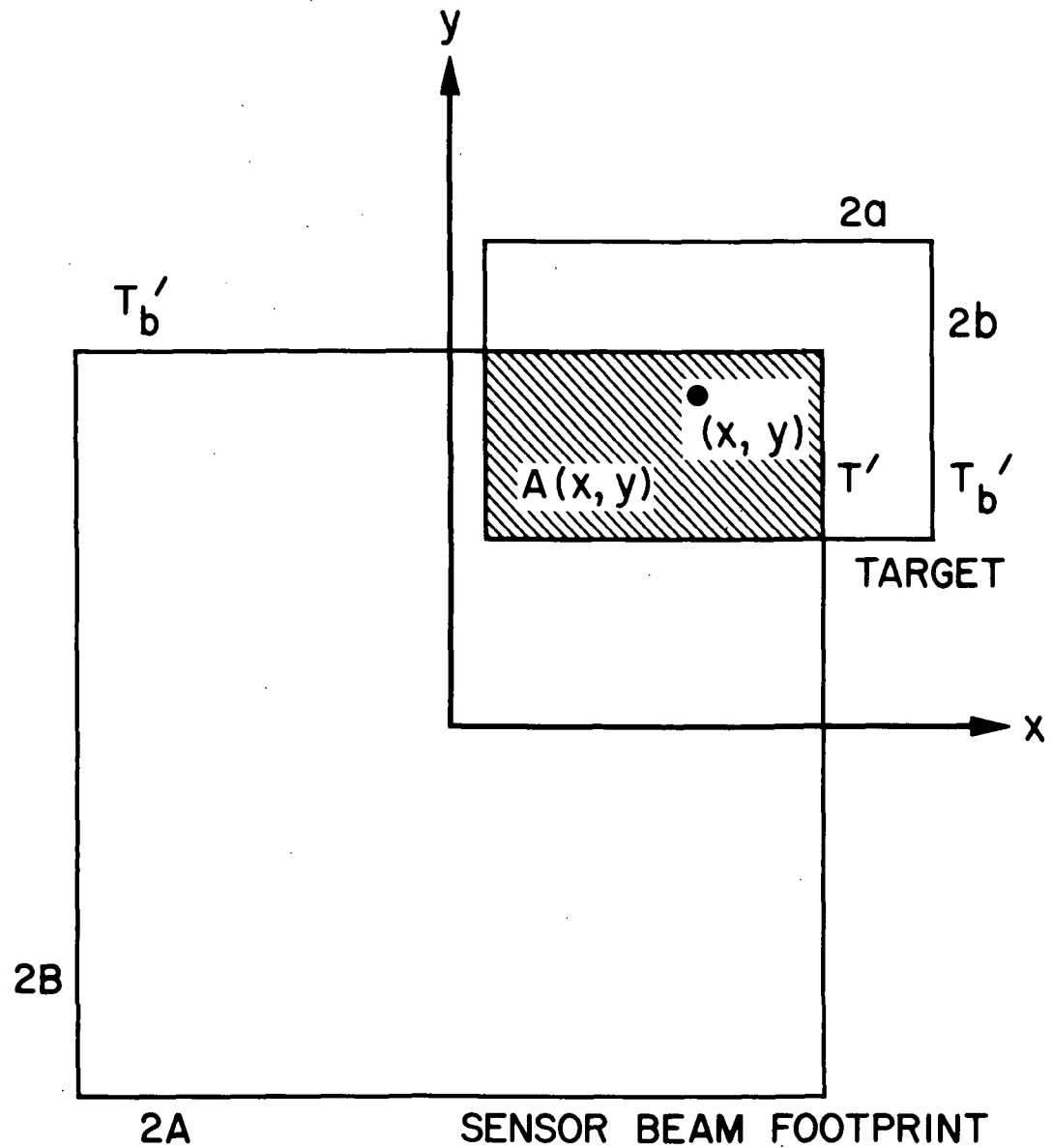


Figure A2